OSCILLATORY AND STREAMING FLOWS IN MICROCHANNELS

BY

GIRIDAR VISHWANATHAN

THESIS

Submitted in partial fulfillment of the requirements
for the degree of Master of Science in Mechanical Engineering
in the Graduate College of the
University of Illinois at Urbana-Champaign, 2019

Urbana, Illinois

Adviser:

Assistant Professor Gabriel Juarez

Abstract

Microfluidics is the study of liquid flow in the small scale (10-1000 μm) channel networks and is widely used in chemistry and biology as a platform for analysis, synthesis, and manipulation. The construction, validation and performance characterization of an oscillatory driver capable of producing oscillatory flow in microfluidic channels in the frequency range 10-1000 Hz is detailed. The application of micro-scale oscillatory flows is broadly divided into two categories. The first using the time reversing nature of the flow for decreasing device size or for prolonged optical observation and the second involving the use of steady secondary rectified flows that arise due to fluid inertia. Both of these application categories are shown to be effectively realizable in this frequency range through the demonstration of inertial particle focusing in the former and microscale mixing in the latter. Additionally, the particular case of steady rectified flows originating from a rigid cylindrical boundary or steady streaming as it is commonly known is used to perform a probe-free optical measurement of the kinematic viscosity of Newtonian liquids. This is followed by a study of steady streaming flows in well-characterized model viscoelastic liquids of two kinds: namely the Boger fluid and the fractional Maxwell liquid. The streaming flow. Steady streaming velocity profiles in elastic liquids with strong shear thinning (fractional Maxwell liquids), however, display two unique features in the confined microfluidic system: (i) a non-monotonic evolution of the inner streaming layer with increasing frequency, first growing then decreasing in width, and (ii) a clear asymmetry in the flow profile at high frequencies.

Acknowledgments

I would like to thank my advisor, Dr. Gabriel Juarez, who has supported and guided me through the course of my Master's degree. I would also like to thank Dr. Luca Martinetti for helping me with rheological measurements as well as lending me his wisdom and Mr. Tejaswin Parthasarathy and Dr. Mike Garcia for insightful discussion.

Table of Contents

List of Tables

List of Figures

List of Abbreviations

THD	Total Harmonic Distortion.
FWHM	Full Width Half Maximum.
ppm	Parts per million.
DI	Deionized water.
gly	Glycerol solution.

List of Symbols

f	Fluid oscillation frequency.
ω	Angular frequency.
μm	Micrometers.
μL	Microliters.
W	Microchannel width.
H	Microchannel height.
L	Microchannel length.
ν	Kinematic viscosity of liquid.
μ	Dynamic viscosity of liquid.
ρ	Density of liquid.
x	Streamwise particle position.
y	Spanwise particle position.
t	Time elapsed.
d	Particle diameter.
U	Streamwise velocity.
U_{max}	Streamwise velocity amplitude.
a	Cylinder radius.
s	Oscillation amplitude.
ϵ	Non-dimensional amplitude.
δ	Stokes boundary layer thickness.
Re	Reynolds number.
L_e	Eddy center length.
ΔP	Channel excess pressure.
D_h	Hydraulic diameter.
Re_p	Particle Reynolds number.
L_f	Focusing length.
C_l	Lift coefficient.
U_m	Maximum microchannel flow velocity.
η	Steady shear viscosity.
$\dot{\gamma}$	Rate of shear.
λ	Polymer solution relaxation time.
R	Universal gas constant.
T	Absolute Temperature.
M_w	Polymer molecular weight.
De	Deborah number.
G'	Elastic modulus.
G''	Viscous modulus.
S	Reynolds material function.
V	Deborah material function.
L_m	Mixing Length.
Pe	Peclet number.
U_a	Average microchannel flow velocity.

Chapter 1

Literature Review

1.1 Microfluidic oscillatory flows: applications

Oscillatory flows in microfluidic devices have been shown to be useful in a range of applications such as rapidly mixing liquids at low Reynolds numbers [Phelan et al., 2008, Ahmed et al., 2009, Frommelt et al., 2008], particle sorting and focusing [Thameem et al., 2016, Schmid et al., 2014, Marmottant and Hilgenfeldt, 2003, Mutlu et al., 2018], enhancement of heat transfer [Qu et al., 2017], flow control [Leslie et al., 2009, Phillips et al., 2016], and chemical extraction [Lestari et al., 2016, Xie et al., 2015]. These may be broadly divided into two categories. The first category of flows are those where oscillatory motion enables instantaneous local velocities or shear rates without net displacement, implemented to reduce device footprint and allow for prolonged observation [Jo et al., 2009, Alizadehgiashi et al., 2009, Mutlu et al., 2018, Abolhasani and Jensen, 2016]. These usually involve oscillatory flows of low frequencies (0.1-10 Hz) and large amplitudes and are particularly useful in biological and bimedical applications because of the reduced exposure to prolonged pressure and shear rate which can damage delicate analytes. The second category of flows are those that utilize steady rectified flows associated with an underlying primary oscillatory flow [Riley, 2001] near boundaries or interfaces. Such flows are normally realized in the presence high frequency oscillations (0.1 - 1000) kHz of small amplitude and have been shown to be useful in mixing [Ahmed et al., 2009], hydrodynamic manipulation of particles and cells [Lutz et al., 2006b, Lieu et al., 2012, Thameem et al., 2016], and more recently, by us as discussed in chapter 6 and 7, in microrheology [Vishwanathan and Juarez, 2019b,

Vishwanathan and Juarez, 2019a].

1.2 Microfluidic oscillatory flows: generation

At low frequencies ($0.1 \leq f \leq 10$ Hz), oscillatory flows are usually achieved by a programmed syringe pump, electromechanical relay valves [Abolhasani and Jensen, 2016] or a pneumatic pressure controller [Zhou and Schroeder, 2016]. The fidelity of the desired waveform is limited by inertia of the oscillatory driver. For low frequencies, the response time of syringe pumps and actuators in electromechanical valves and pnuematic pressure controllers is on the order of $\mathcal{O}(10$ ms), therefore preventing the realization of sinusoidal oscillations at higher frequencies.

At high frequencies ($10^3 \leq f \leq 10^6$ Hz), piezoelectric transducers, which typically possess resonant frequencies in this range, are used [Rallabandi et al., 2017, Phillips et al., 2016, Xie et al., 2015, Lieu et al., 2012, Morris and Forster, 2000]. At these frequencies, effects are usually local to the transducer and are effected through the use of rigid boundaries, interfaces or bubbles which serve to amplify their effect within a microfluidic device. The utility of piezoelectric transducers in the 10 - 1000 Hz range are limited by the small amplitudes generated. The amplitudes may be partially increased through the use of designed features such as membrane cavities in the channel on to which the piezo elements need to be bonded to be used properly [Vázquez-Vergara et al., 2017]. More recent designs of microfluidic oscillators primarily aim to achieve oscillatory flows free of external actuators with a focus on miniaturization and integration with other lab-on-chip modules. This is typically done by exploiting non-linear fluid-elastic interaction with a membrane or diaphragm unit as a steady flow is driven through it. Therefore, a time dependent response is obtained even with a steady input at low Reynolds numbers [Xia et al., 2012, Leslie et al., 2009, Kim et al., 2013, Mosadegh et al., 2010]. Other possibilities such as the use of non-Newtonian fluids for switching [Groisman et al., 2003], generation of oil droplets

as an oscillatory source [Basilio et al., 2019], and the Coanda effect [Yang et al., 2007] have also been explored. Although these micro-oscillators are highly miniaturized, modular and in some cases, capable of producing frequencies in the audible range [Xia et al., 2012], they mostly require the fabrication of complex MEMS devices potentially discouraging their use in research attempting to use oscillatory flows. Further, in microfluidic oscillators that function based on fluid elastic interaction the amplitudes and frequencies are coupled and hence cannot be independently controlled.

This thesis details the construction of a simple speaker based setup capable of producing highly sinusoidal flow in the intermediate frequency regime (10-1000 Hz) with an independently controllable amplitude in the range 10-1000 μm. Its performance is characterized and a validation of the resulting flow against theoretical expectations is performed. The applications of oscillatory flow are explored in both typical categories, that is, by using the oscillatory nature of flow for inertial particle focusing in a straight channel and the steady secondary flows for microscale mixing of two liquids. Additionally, the steady secondary flows created by a no-slip solid cylindrical boundary or steady streaming, is realized and applied to visually obtain the kinematic viscosity of Newtonian liquids. The use of steady streaming around a cylinder for microrheology is further explored by studying the flow profile of streaming vortices with frequency for model viscoelastic liquids.

1.3 Microrheology

Microrheology aims at measuring local material properties of small quantities (μL - nL) of fluids by studying the relationship between deformation and stress. Optical microrheology techniques rely on the tracking of flow tracers under passive thermal fluctuations or active external forcing [Waigh, 2005, Squires and Mason, 2010, Wilson and Poon, 2011, Zia, 2018]. The development of microrheological methods for complex fluids and soft materials [Pipe and McKinley, 2009, Waigh, 2016] has been motivated by the advantages of-

fered by microfluidic devices compared to conventional bulk techniques. Advantages include small sample volume, reduction of free-surface effects, direct visualization of the underlying microstructure, and the ability to quantify low-viscosity and weakly viscoelastic solutions [Giudice et al., 2017a, Giudice et al., 2017b]. These specialized methods have been shown to measure material properties such as the steady shear viscosity [Gupta et al., 2016], the most widely characterized material property, as well as the extensional viscosity [Haward, 2016], [Galindo-Rosales and Alves, 2013], and the longest relaxation time [Giudice et al., 2015], [Zilz et al., 2014] of various fluids. Here we present a method to measure the kinematic viscosity of Newtonian liquids optically using the flow profiles arising from steady streaming.

1.4 Steady Streaming

Steady streaming flows have received a renewed interest over the past decade due to their numerous applications in microfluidic devices [Friend and Yeo, 2011, Wiklund et al., 2012]. Here, steady streaming refers to the rectified flow [Riley, 2001] that occurs near the boundary of a rigid cylinder of radius a, in an oscillating liquid with frequency f and small-amplitude s ($\ll a$), in a stationary incompressible fluid of kinematic viscosity ν. The magnitude of the characteristic streaming velocity scales as $U_s \sim \epsilon s\omega$, where $\epsilon = s/a$ is the dimensionless amplitude and $\omega = 2\pi f$ is the angular frequency. At small scales, these rectified flows have been shown to be useful in non-contact manipulation [Amit et al., 2016], trapping [Marmottant and Hilgenfeldt, 2003, Lutz et al., 2006a, Lieu et al., 2012], [Yazdi and Ardekani, 2012] and sorting [Wang et al., 2011, Thameem et al., 2017] of particles and cells as well as in enhancing pumping [Girardo et al., 2008] and mixing [Sritharan et al., 2006, Lutz et al., 2006b, Ahmed et al., 2009] at low Reynolds numbers. There are opportunities to use steady streaming for the rheology of liquids as well [Vlassopoulos and Schowalter, 1993].

The steady streaming regime of an oscillating cylinder [Wang, 1968, Chong et al., 2013,

Coenen, 2016] is dictated by the magnitude of the Reynolds number, $\mathrm{Re} = \omega a^2/\nu$, and the streaming Reynolds number, $\mathrm{Re_s} = \omega s^2/\nu$. Microscale streaming flows and applications have previously focused on ultrasonic frequencies and above ($f \geq 10$ kHz), typically induced by the interaction between a liquid and surface acoustic waves generated by piezoelectric transducers [Friend and Yeo, 2011, Yeo and Friend, 2009]. The streaming regime associated with high frequencies and streaming Reynolds numbers greater than unity ($\mathrm{Re_s} > 1$) is that of a double streaming layer; an inner driving layer and an outer driven layer of the opposite sense. At high frequencies, the inner streaming region is confined to a thin layer near the cylinder surface making experimental studies of the inner region challenging and therefore less common [Coenen, 2016]. By utilizing sub-kHz oscillation frequencies, our experiments constrain the streaming Reynolds number to always be less than unity ($\mathrm{Re_s} < 1$), ensuring that the inner streaming layer is comparable in size to the cylinder radius allowing proper resolution and measurability as compared to streaming flows in the $\mathrm{Re_s} > 1$ regime. Because the inner boundary layer thickness scales as $\delta \sim \sqrt{\nu/\omega}$, our approach characterizes the evolution of the inner streaming boundary layer as a function of oscillation frequency with standard particle tracking techniques.

Dramatic changes in the steady streaming flow field of dilute polymer solutions around a cylinder oscillating at low frequencies ($10 \leq f \leq 100$ Hz) were experimentally observed [Chang and Schowalter, 1974]. In contrast to the Newtonian case, the inner streaming layer in non-Newtonian liquids was found to grow in size with increasing frequency, eventually displacing the outer driven vortices completely and giving the appearance of a reversed flow [Chang and Schowalter, 1979]. The growth of the inner streaming layer was theoretically described using viscoelastic constitutive models [Frater, 1967, Chang, 1977, James, 1977, Böhme, 1992], however, few studies have investigated the link between the steady streaming flow and the measured rheological properties of non-Newtonian liquids. One such study used steady streaming as a rheological tool to characterize drag-reduction in dilute polymer solutions [Vlassopoulos and Schowalter, 1993]. While a qualitative correlation between the

drag reduction performance and the liquid relaxation time was observed, inconsistencies in the measured relaxation times from steady streaming differed by two orders of magnitude when compared to estimates from steady shear rheology. This key observation implied that the longest relaxation time may not be the important characteristic time when considering steady streaming in non-Newtonian liquids.

Chapter 2

Experimental setup and methods

The apparatus is set up as displayed in the schematic, shown in Figure 2.1 (a). A PDMS microchannel is bonded to a glass slide and observed through an inverted microscope. A loudspeaker (DROK TDA7297B, 15 W, 90 dB) is mounted next to the microscope stage. The oscillation frequency and amplitude (volume) of the loudspeaker diaphragm are controlled by a computer via an auxiliary cable. One end of microfluidic tubing (PE60 Intramedic 427416, 0.76 mm ID $\times$ 1.22 mm OD) is directly attached to the diaphragm of loudspeaker while the other end is inserted into the microchannel outlet. The tubing is maintained taut and its boundary conditions correspond to a fixed end at the microchannel outlet and a forced oscillatory displacement at the diaphragm. The microchannel and the tubing are filled with liquid during operation. The oscillatory displacement of the diaphragm is transduced into elastic deformations of the microfluidic tubing at the fixed end of the device outlet. The stress induced by tubing deformation generates a time-varying pressure within, resulting in oscillatory displacement of the liquid at the same frequency (f) as the diaphragm. The streamwise displacement of a tracer particle in the channel is described by $x = s\cos(\omega t + \phi)$ and illustrated in Figure 2.1 (b). Here, s oscillation amplitude, ω is the angular frequency, and ϕ is the initial phase.

To characterize the oscillatory flow in microchannels, tracer particles at the midplane of the microchannel were observed using brightfield illumination with objectives of 10$\times$ and 20$\times$ magnification (depth of field 8.5 μm and 5.5 μm respectively). To ensure that the tracers accurately represented the flow, polystyrene tracer particles with a mean diameter of 0.93 μm and density of 1.08 g/cm^3 were suspended in deionized water (unless mentioned

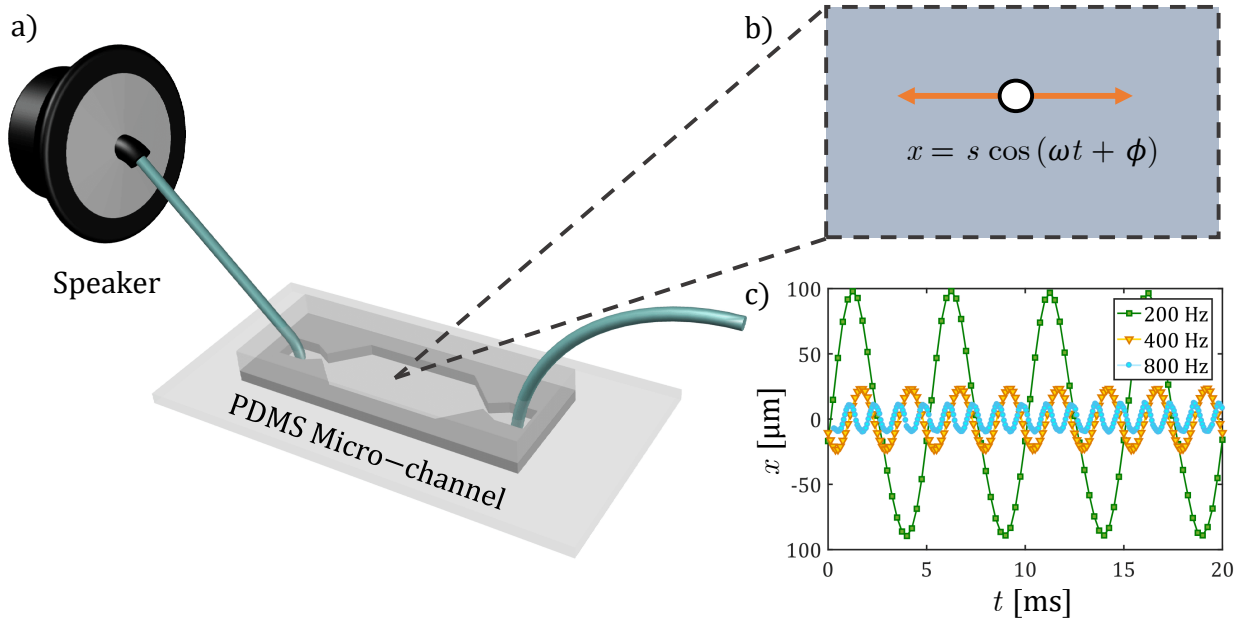

Figure 2.1: (a) Schematic of the experimental setup. The loudspeaker diaphragm is directly interfaced with microfluidic tubing (maintained taut and filled with liquid) to generate sinusoidal liquid oscillations in a PDMS microchannel. (b) Schematic of tracer particle (and liquid) displacement in a microchannel described by the oscillation amplitude and angular frequency. (c) Experimental streamwise displacement of 0.93 μm diameter tracer particles in water over a number of oscillation cycles obtained with micro-particle tracking velocimetry.

otherwise). The response time associated with the tracer particles ($\tau = \rho d^2/18\mu \approx 50 \times 10^{-9}$ s) is much smaller than the oscillatory timescales considered in this study ($\tau \ll 1/f$). The oscillatory displacement of the particle positions were recorded using a high-speed scientific CMOS camera (Edgertronic® SC2+) with frame rates exactly twenty times larger than the driving oscillation frequency ($20f$). The long time tracking of a steady streaming flow profile or inertial particle was performed stroboscopically using framerates that are equal to or perfect divisors of the oscillation frequency by a high resolution global shutter CMOS camera (XIMEA® XiQ). The displacement and velocity fields are then obtained from 2D particle tracking velocimetry algorithms.

PDMS microchannels were produced from a SU-8 patterned master silicon wafer. The microchannel geometries used were the following: (i) a square channel with a width and height of 110 μm and length of 5 cm, (ii) a rectangular channel with a width of 5 mm, height of 200 μm, and length of 2 cm, and (iii) a cross slot channel with square cross section with a width and height of 110 μm (iv) rectangular channels with a width of 5 mm, height of 200 μm, and length of 2 cm with a single cylindrical protrusion at the geometric center of radius a, where $a = 100,\ 200,\ 300,\ 400\ \mu$m .

Chapter 3

Characterization and validation

Examples of streamwise displacement of individually tracked particles from their mean position over a number of cycles during a 20 ms period are shown in Figure 2.1 (c). The ratio of sampling frequency (camera framerate) to liquid oscillation frequency is kept constant at 20. That is, for oscillation at 200, 400 and 800 Hz, a framerate of 4000, 8000 and 16000 Hz is used, respectively. The corresponding amplitudes are 100, 27 and 14 μm.

The independent operational range between amplitude and frequency is shown in Figure 3.1 (a). For a given frequency, the displacement of a tracer particle is dependent on the volume setting of the loudspeaker. As an example, three volume settings are considered here: low (30%), intermediate (60%), and high (90%), where the percentages correspond to the maximum speaker volume as determined by the computer. At 100 Hz, for example, the amplitude ranges from 50 μm at low to 800 μm at high volume setting. The amplitude swept by a tracer particle over a single oscillation period, for a given volume setting, shows a non-monotonic variation with frequency. Owing to the performance characteristics of the speaker, the maximum oscillation amplitude occurs at 200 Hz, which corresponds to the resonant frequency ($\approx$ 230 Hz) of the loudspeaker diaphragm. The horizontal black line indicates the maximum particle oscillation amplitude of 800 μm that can be measured due to the field of view limited by the camera when using a 10$\times$ microscope objective lens.

A Fourier spectrum analysis of particle trajectories at varying oscillation amplitudes and frequencies is shown in Figure 3.1 (b). The spectra have been obtained for oscillation frequencies of 50, 200 and 800 Hz and at volume settings of low, intermediate, and high. For low and intermediate volume settings, monodisperse peaks in the spectral intensity

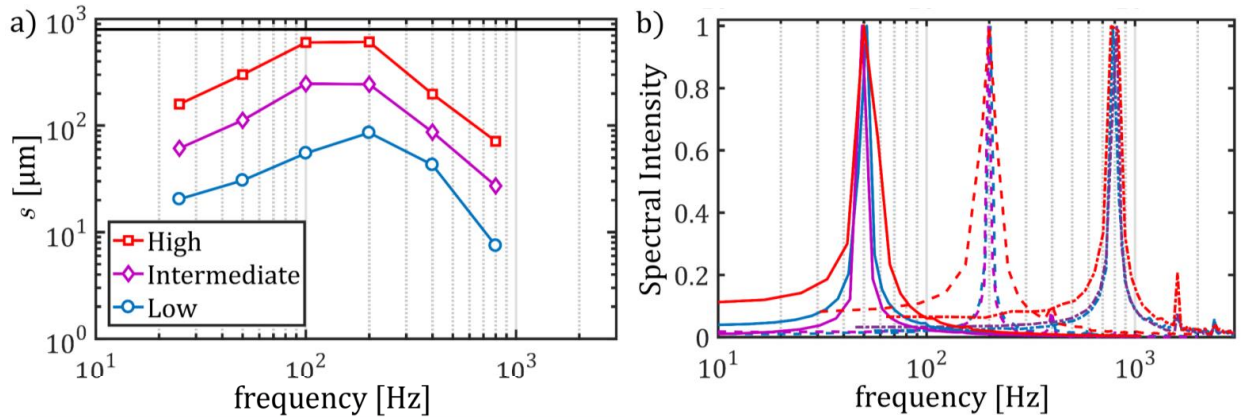

Figure 3.1: (a) The amplitude of oscillatory displacement in microchannels for a range of frequencies and three amplitudes, or speaker volume settings, of low (30%, blue), intermediate (60%, magenta) and high (90%, red). (b) Fourier spectrum analysis of tracer particle displacement in the streamwise direction at three different frequencies (50, 200, and 800 Hz) and amplitudes (low, intermediate, and high).

correspond to the input driving frequency of the loudspeaker. The peaks are especially narrow at 200 Hz, or near the resonance frequency of the diaphragm. For high volume settings, the peaks correspond to the input driving frequency, however, widening of the peak is noticeable. In some cases, such as for 800 Hz at high volume setting, contributions due to higher harmonics are of considerable strength.

A quantitative measure of harmonic distortion present in the signal as compared to the fundamental driving frequency is obtained by calculating the total harmonic distortion (THD). The THD is defined as THD $= \sqrt{\Sigma_{i=1}^{N} V_i^2}/V_1$, where V_i is the power of the spectral intensity at the ith harmonic [Shmilovitz, 2005]. A low THD value is associated with a more accurate representation of the original driving signal. For low volume settings, the THD at 50, 200, and 800 Hz are 3.5%, 7.1%, and 9.1%, respectively. For intermediate volume settings, the THD at 50, 200, and 800 Hz are 5.2%, 8.9%, and 13.4%, respectively.For high volume settings, the THD at 50, 200, and 800 Hz are 7.3%, 11.1%, and 21.3%, respectively. The growing magnitude of higher harmonics with increasing speaker volume typically limits operation at frequencies $>$ 400 Hz to low or intermediate speaker volumes. At low frequencies however, the maximum amplitude is chosen to avoid damage to the microchannel or

unfastening of the outlet tube from the speaker cone. Therefore, sinusoidal oscillations with amplitudes ranging from $10 < s < 200$ μm can be reliably achieved throughout the entire range of frequency.

The maximum pressure inside the square channel may be estimated from the modified Poiseuille formula:

$$\Delta P = \frac{64 \mu L s f}{D_h^2} \ , \tag{3.1}$$

where D_h and L are the hydraulic diameter and length of the channel. For the square channel ($D_h = 110$ μm and $L = 5$ cm) filled with DI water ($\mu = 1.002$ mPa s) and settings for maximum oscillatory displacement ($f = 200$ Hz, $s = 600$ μm), the pressure inside the channel is calculated to be approximately equal to 31 kPa.

The small length scales of $\mathcal{O}(100$ μm) associated with microchannels imply that most microscale flows are laminar flows governed by the Stokes equation. An important feature of microscale oscillatory flows in the $10-1000$ Hz range is that transient effects associated with the unsteady Stokes equation become significant. An example of departure from Stokes flow is illustrated by the comparison of the steady Stokes flow velocity profile [O'Brien, 1975] at the midplane (black solid curve) against those obtained experimentally for oscillatory flow at different frequencies (symbols), shown in Figure 3.2 (a).

To obtain the amplitude of velocity in the square channel midplane, $50 - 200$ particles (0.93 μm diameter) are tracked for one hundred oscillation cycles and their respective velocities are computed. The amplitude of each velocity series ($U_{max}(y)$) is obtained and superposed in the streamwise direction. The resulting spread of speeds is filtered for outliers and averaged. The associated statistical error bars are smaller than the data markers shown.

The results for 100 Hz and 400 Hz are similar to the Stokes laminar flow profile (black solid curve). At 800 Hz, however, there is considerable deviation from the steady velocity profile due to increasing W/δ with frequency. For the cases of 100, 400, and 800 Hz the W/δ values are 2.75, 5.51, and 7.78, respectively. For these W/δ values, the analytical

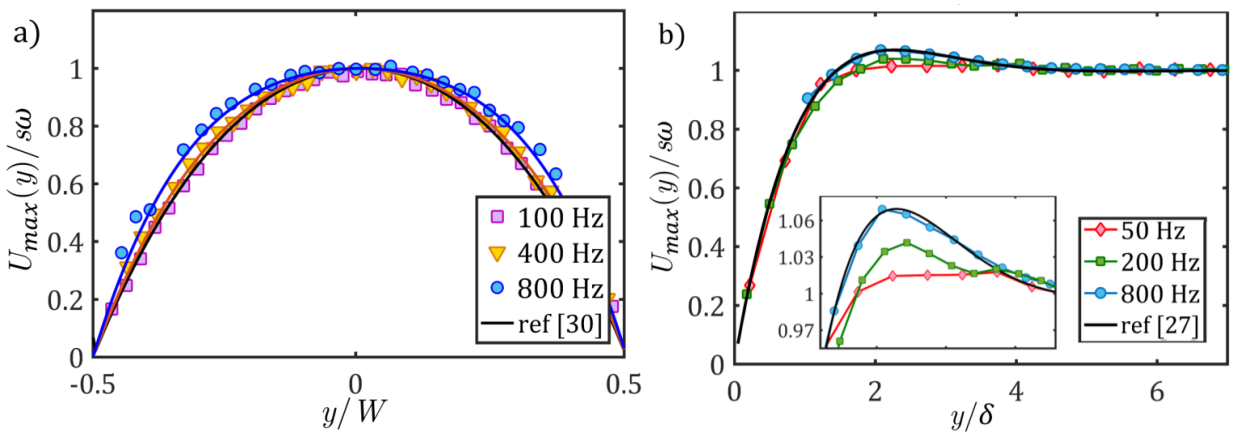

Figure 3.2: (a) Oscillatory velocity flow profile in a square channel (symbols) showing deviation from Stokes flow profile (black solid curve) with increasing frequency. (b) Oscillatory velocity profile with position (symbols) near a solid channel wall in a semi-infinite rectangular channel ($W \gg H$) showing agreement with the theoretical solution (black solid curve) to Stokes' second problem [Landau and Lifshits, 1959] with increasing frequency. (Inset) Close-up of the region from $1.5 \leq y/\delta \leq 4.5$ to demonstrate agreement with equation (3.2) at different frequencies.

series solution for the amplitude of the midplane oscillatory velocity profile ($U_{max}(y)$) was evaluated correct to one hundred terms [O'Brien, 1975], and are shown by the continuous lines to good agreement with experimental data, even at 800 Hz.

In contrast, deviations from the unsteady Stokes equation are demonstrated in Figure 3.2 (b) by comparing the amplitude of measured oscillatory flow (symbols) in the rectangular channel ($W \gg H$), with those obtained theoretically from the solution to oscillatory flow over an infinite flat plate (Stokes' second problem) [Landau and Lifshits, 1959, Wang, 1989]. The maximum temporal flow velocity as a function of distance from a flat plate is given by the expression:

$$U_{max}(y)/s\omega = \sqrt{2}e^{-y/(2\delta)}\sqrt{\cosh(y/\delta) - \cos(y/\delta)}\ , \tag{3.2}$$

where δ is the Stokes boundary layer length and equal to $\sqrt{\mu/\rho\omega}$. At 800 Hz, normalized experimental data (symbols) is in good agreement with equation (3.2). At 50 Hz, and to a lesser extent at 200 Hz, deviations from the theory occur where the velocity amplitudes are larger than those at the far field and is detailed in the inset. This is due to the relatively

short channel height (200 μm) and the effect of boundary layers at the top and bottom walls of the channel affecting flow at the midplane. The corresponding values of W/δ for the cases of 50, 200, and 800 Hz are 3.57, 7.14, and 14.3, respectively. Therefore, at the midplane, effects of channel side-walls may be neglected for distances larger than 4δ into the channel. Further, three dimensional flow effects can be ignored for $W/\delta \geq 7.5$ when the shorter dimension is used.

Chapter 4

Oscillatory focusing of inertial particle

Inertial focusing in microchannels is a passive technique where suspended particles undergoing unidirectional flow migrate across streamlines, due to particle inertia, to equilibrium focus positions [Di Carlo et al., 2007, Di Carlo, 2009, Martel and Toner, 2014]. In straight channels, of rectangular or circular cross section, the competing forces that lead to particle migration are the wall interaction force, which directs the particle away from the channel wall, and the shear gradient force, which directs the particle toward the channel wall. The summation of these forces is termed the inertial lift and the equilibrium position of the particle is determined once the opposing forces are balanced. Factors influencing the inertial lift force are the channel geometry, flow rate, and particle size. Since it is a high-throughput method for non-contact manipulation at the microscale, inertial focusing has been utilized in numerous applications ranging from flow cytometry [Hur et al., 2010, Bhagat et al., 2010], [Oakey et al., 2010] size sorting [Kuntaegowdanahalli et al., 2009, Wu et al., 2012] , mixing [Amini et al., 2012], and filtration [Seo et al., 2007]. An important parameter when designing channels for applications is the length required to reach the equilibrium focus position, estimated [Di Carlo, 2009] to be equal to

$$L_f = \frac{4\pi\mu D_h^2}{\rho U_m d^2 C_\ell} \ , \tag{4.1}$$

where U_m is the maximum flow velocity and C_ℓ is the lift coefficient, which typically varies in the range of $0.02-0.05$. From this relation, it is apparent that sufficiently high velocities and large particles are required to minimize the focusing length. Recent work, however, demon-

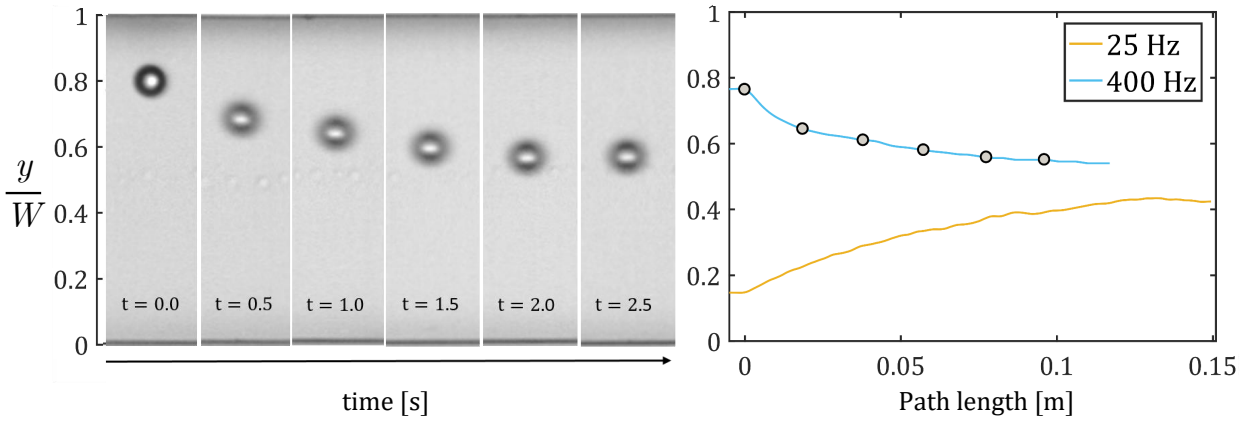

Figure 4.1: (a) Inertial focusing of a 10 μm polystyrene particle in oscillatory flow with a frequency of 400 Hz in a 110 μm square channel. (b) The spanwise location of the particle centroids as they migrate to the equilibrium position at the center of the channel during oscillatory flow.

strates the use of oscillatory flows for inertial focusing, where oscillatory flow at relatively low frequencies (< 20 Hz) results in a channel of practically infinite length [Mutlu et al., 2018]. Thus, it becomes possible to focus particles with far smaller particle Reynolds numbers corresponding to $\mathrm{Re_p} = (d/2W)^2\mathrm{Re} < 0.01$.

Inertial focusing of a 10 μm polystyrene particle in oscillatory flow of 400 Hz with an amplitude of 22 μm is demonstrated in the square channel, for which, $\mathrm{Re_p} = 0.050$ and $d/W = 0.182$. Micrographs of a single polystyrene particle at regular time intervals as it migrates to the equilibrium position is shown in Figure 4.1 (a). Using stroboscopic imaging, the lateral migration toward the center of the channel is apparent. The corresponding vertical position of the particle centroid, as determined by particle tracking, is shown as a function of the approximate path length traversed by the particle in Figure 4.1 (b). The marked points (symbols) correspond to the instances shown in the micrographs. The path length is estimated as $4sft$, where $4s$ is the distance covered by the particle at the center of the channel in a single oscillation cycle and t is the time elapsed after the start of oscillations. The focusing behavior of another particle at 25 Hz and an amplitude of 36 μm is also shown. The corresponding path length for focusing (or focus length) is found to be about

0.15 m, comparable to the 400 Hz case and in good agreement with previous results for similar conditions ($\mathrm{Re_p} = 0.050$ and $d/W = 0.25$) [Mutlu et al., 2018]. The time required for focusing, however, is about 3 seconds for the 400 Hz case and 35 seconds for the 25 Hz case.

The advantages of oscillatory flow for inertial focusing include decreased channel lengths, lower pressure drops, and lower shear rates. Because there is no net displacement, the particle remains in the field of view as it migrates to the equilibrium position. In contrast with unidirectional flow, the approximate channel length required for the particle to reach it's equilibrium position as determined by equation (4.1), where U_m is given by the characteristic fluid velocity $s\omega$, is $L_f \approx 1.37$ m, which is impractical. The lower pressure drop allows for the convenient fabrication and use of PDMS microchannels. The combination of lower pressure drop and lower shear rates is of particular interest in biomedical application where cells are susceptible to damage induced by fluid stresses.

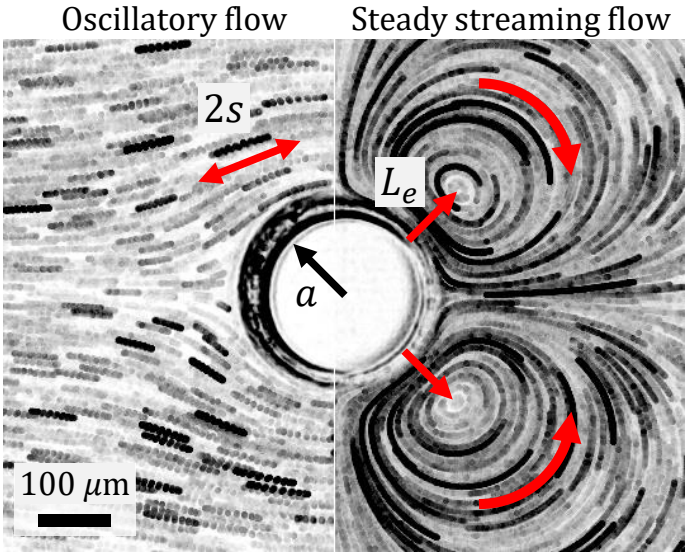

Figure 4.2: Steady streaming around a cylindrical obstacle in a microfluidic device. (Left) Pathlines of tracer particles captured with high-speed imaging. The displacement amplitude of $2s$ is shown as the fluid undergoes one period of oscillation. (Right) Pathlines of tracer particles captured with stroboscopic imaging. Half of the steady streaming profile is shown with two counter-rotating vortices and the location of the eddy center, L_e. Here, the cylinder radius is $a = 100$ μm.

Chapter 5

Mixing with steady secondary flows

Low Reynolds number (Re $\leq$ 1) flow in microchannels present a significant challenge to applications involving mixing [Ottino and Wiggins, 2004]. This is because, the dominant mechanism of mixing is diffusion in the absence of chaotic advection, which is normally associated with high Re mixing. The effectiveness of mixing is quantified by estimating the length required to achieve mixing (L_m). For purely diffusive mixing,

$$L_m \geq D_h \mathrm{Pe} \ . \tag{5.1}$$

Above, Pe is the Peclet number and defined as the ratio of $U_a W/D$, where U_a is the average flow velocity and D is the diffusion coefficient. For Re $\leq$ 1 and diffusion coefficients of $D \approx 100\ \mu\mathrm{m}^2\ \mathrm{s}^1$, the Peclet number would be Pe $\geq 10^4$, resulting in a channel length for sufficient mixing to be $L_m \geq 1$ m, which is undesirable.

To overcome this challenge, a variety of microscale mixers have been developed to enhance mixing at low Re, and are categorized as either passive or active mixers [Hessel et al., 2005, Nguyen and Wu, 2005, Lee et al., 2011, Ward and Fan, 2015, Lee et al., 2016, Cai et al., 2017]. Passive mixers make use of the channel geometry, usually incorporating repeating complex or 3D channel features to enhance mixing of two streams flowing together at a constant rate. On the other hand, active mixers rely on externally applied forces and are further categorized based on the nature of the external actuation [Ober et al., 2015]. One such category of mixers are acoustic micromixers [Liu et al., 2002, Ahmed et al., 2009, Bachman et al., 2019] that rely on external acoustic actuation to generate steady rectified flows that mix different

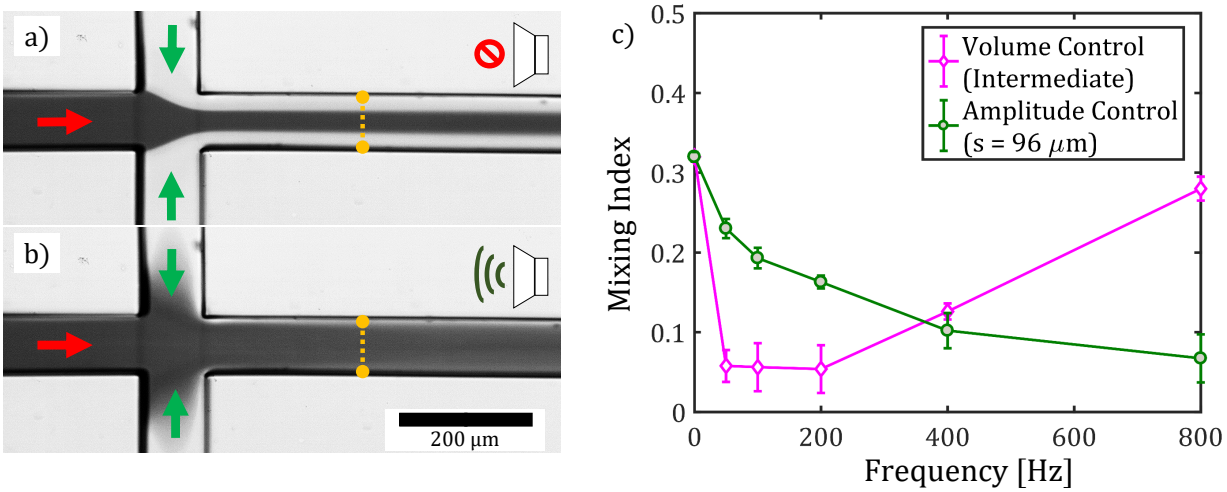

Figure 5.1: (a) Mixing of co-flowing streams of 30% (w/w) aqueous glycerol solutions without oscillations applied. (b) Mixing of co-flowing streams of 30% (w/w) aqueous glycerol solutions with oscillations applied at a frequency of 400 Hz. (c) Mixing index as a function of frequency for constant amplitude and constant volume settings measured at a distance $2.5W$ downstream from the cross-slot region. Scale bar is 200 μm.

liquids.

Here, mixing of two aqueous glycerol solutions (30% w/w, μ = 2 mPa s), one with colored dye and one without, is demonstrated in the cross-slot channel using steady rectified flows. As seen from figure 5.1 (a), the dyed solution enters the cross-slot with a flow rate of 0.3 μL/min (red arrow) while the undyed solution enters the cross-slot from either side with identical flow rates of 0.15 μL/min (green arrows). This results in a total flow rate of 0.6 μL/min at the outlet.

When no oscillatory flow is imposed, minimal diffusive mixing at the interface is observed within the field of view. When oscillatory flow of 400 Hz is imposed on the same configuration, steady vortices are generated near the corners of the cross-slot as seen in Figure 5.1 (b), which facilitate mass transfer across the interface through advection. A large exposure time of 20 ms was used for imaging so that variations over signal phase are averaged.

Mixing performance is quantified by first obtaining the intensity profile across the channel at a distance $2.5W$ downstream from the center of the cross slot, indicated by the yellow dashed lines in Figure 5.1 (a) and (b). The standard deviation of the mixture fraction

profile, derived from the intensity values, is used as the mixing index and is defined as $\mathrm{MI} = \sqrt{\Sigma(I_i - I_m)^2/N}$, where, I_i is the pixel intensity value and I_m is the pixel intensity of a completely mixed solution, and N is the number of sampling points [Liu et al., 2000]. The values of the index range from $\mathrm{MI} = 0.5$ for completely unmixed to $\mathrm{MI} = 0$ for completely mixed solutions. A value of $\mathrm{MI} \leq 0.1$ indicates sufficient mixing.

The variation of the mixing index as a function of frequency for both constant oscillation amplitude and constant volume setting are shown in Figure 5.1 (c). For constant amplitude settings, the mixing index decreases monotonically with increasing frequency, implying sufficient mixing for $f \geq 400$ Hz. The improved mixing with increasing frequency is due to the increase in magnitude of the steady rectified flow velocities, which scale as $\mathcal{O}(s^2\omega)$. For a constant volume (intermediate) setting, however, the mixing index is non-monotonic, with sufficient mixing occurring in the range of $100 - 200$ Hz. Based on the amplitude characteristics, shown in Figure 3.1 (a), for constant volume settings, the largest amplitudes occur near the resonance frequency of the loudspeaker diaphragm.

For the specific case presented here, the length demonstrated to achieve good mixing with steady rectified flows ($L_m \leq 250$ μm) is much less than the length required for mixing according to equation (5.1), which is calculated to be $L_m = 2.5$ cm. Although the nature of forces involved are purely hydrodynamic, oscillatory flows with independently controllable amplitude and frequency allow for the decoupling of flow rate from the rate of mixing which is not possible for passive micromixers. Additionally for the range of frequencies and amplitudes achieved here, strong rectified flows are achieved near solid boundaries in the microchannel as opposed to the boundaries of bubbles used with ultrasonic frequencies elsewhere [Liu et al., 2002, Ahmed et al., 2009] which are unstable at long operation times. Lastly, the implementation of this method in combination with any other passive or active technique can further enhance mixing at the microscale by increasing the number of passes without affecting flow rate.

Chapter 6

Newtonian viscometry with steady streaming flows

The steady streaming flow field of an incompressible Newtonian liquid near a PDMS cylinder of radius a is illustrated in Figure 4.2. The oscillation amplitude is determined from the pathlines of individual tracer particles undergoing a single period of oscillation located far from the cylinder, approximately $5a$, where the flow is uniform. An example of a minimum projection image, captured with high-speed imaging, shows the pathlines of tracer particles near the cylinder (Fig. 4.2, left). When viewed stroboscopically, the secondary steady streaming flow component, rather than the oscillatory flow component, is observed. The steady streaming flow has a quadrupolar structure, consisting of four counter-rotating vortices centered a distance L_e normal to the cylinder surface (Fig. 4.2, right). Flow is directed toward the cylinder boundary parallel to the oscillation direction and away from the cylinder boundary perpendicular to the oscillation direction.

The evolution of the steady streaming flow profile with increasing frequency for water is shown in Figure 6.1. The four counter rotating vortices are identified with tracer particle pathlines (Fig. 6.1, top row). The magnitude of the 2D velocity field was obtained by tracking between $500 - 1000$ particles for 1500 frames using standard particle tracking velocimetry (PTV) routines [Ouellette et al., 2006]. Based on the particle seeding concentration, the depth of field, and imaging region of interest, the predicted number of trackable particles ranged between $600 - 1200$ per frame.

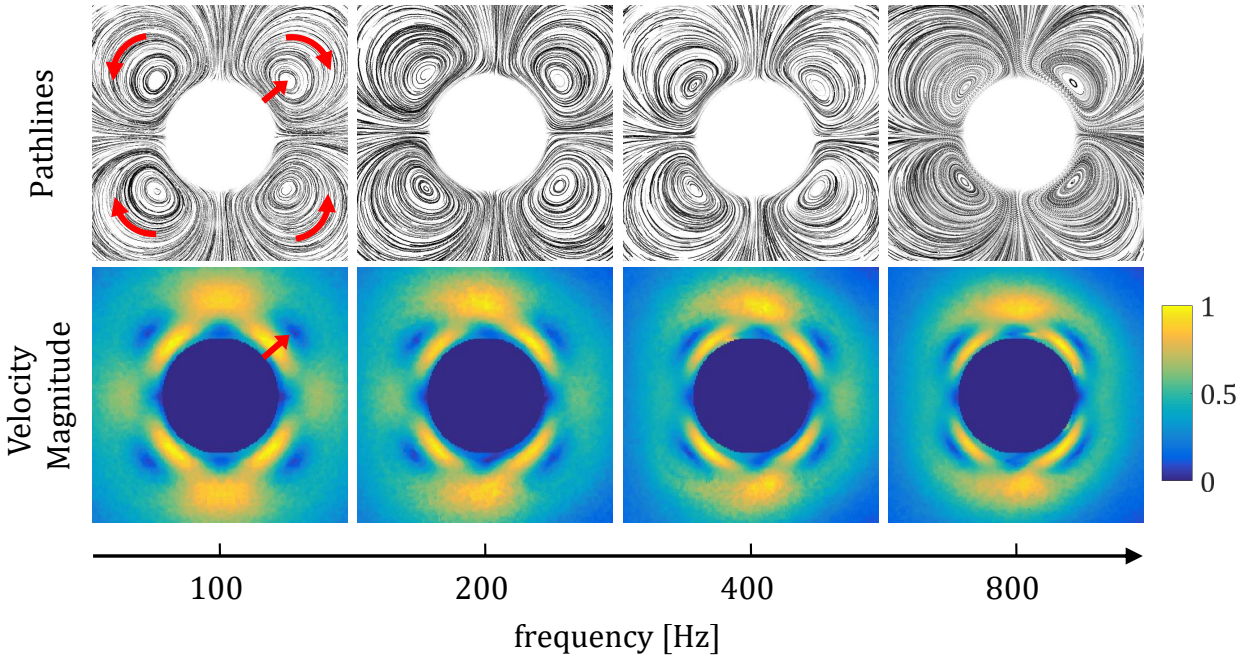

Figure 6.1: Evolution of the steady streaming profile with increasing oscillatory frequency. (top) Pathlines of tracer particles captured with stroboscopic imaging showing the steady streaming profile around a cylindrical obstacle. The location of the eddy center, L_e denoted by the red arrows, moves closer to the cylinder boundary as the oscillation frequency is increased. (bottom) Normalized velocity field magnitude profiles obtained from particle tracking velocimetry (color online).

6.1 Calibration

The location of the central vortices with respect to the cylinder boundary are quantified by the eddy center locations, L_e, which decrease in magnitude with increasing oscillation frequency (Fig. 6.1). The eddy center locations can be determined from custom image analysis routines that identify the cylinder centroid, cylinder boundary, and the location of the local minima of the velocity field with respect to the centroid. Subtracting the value of the cylinder radius determined the value of L_e (Fig. 6.1, 100 Hz bottom row). The eddy center distance can also be determined manually from particle pathline visualizations (Fig. 4.2, right and Fig. 6.1, 100 Hz top row). When eddy center measurements from image analysis routines were compared with manual measurements for DI water, it was found to differ by $< 3\%$. The error in the eddy center measurements for both image analysis routines and manual methods, was taken to be half the difference between the maximum and the minimum of the four eddy center distances. This is an upper estimate for the error as compared to the error across multiple trials since the dominant factors are interference from the channel wall at low frequencies and manufacturing imperfections at high frequencies. Therefore, the streaming patterns, while prone to minor asymmetries, are highly repeatable and insensitive to variations in amplitude.

The dimensionless eddy center location increases monotonically with increasing dimensionless Stokes length (Fig. 6.2 (a)). In this case, the Newtonian liquid used was deionized water with $\nu = 0.949 \times 10^{-6}$ m^2/s. For small Stokes lengths ($\sqrt{\nu/\omega a^2} \leq 0.1$), the dimensionless eddy center increases linearly, in good agreement with theory[Holtsmark et al., 1954] (Fig. 6.2 (a), black dashed line). For larger Stokes lengths ($\sqrt{\nu/\omega a^2} \geq 0.1$), the location of the dimensionless eddy center diverges from the linear behavior and approaches a fixed value of L_e/a. The plateau behavior is attributed to the interaction of the streaming vortices with the finite width of the microfluidic channel walls. It was previously shown that when $\sqrt{\nu/\omega a^2}$ is in the range of $0.16 - 0.18$, the outer boundary distance of the streaming vortices

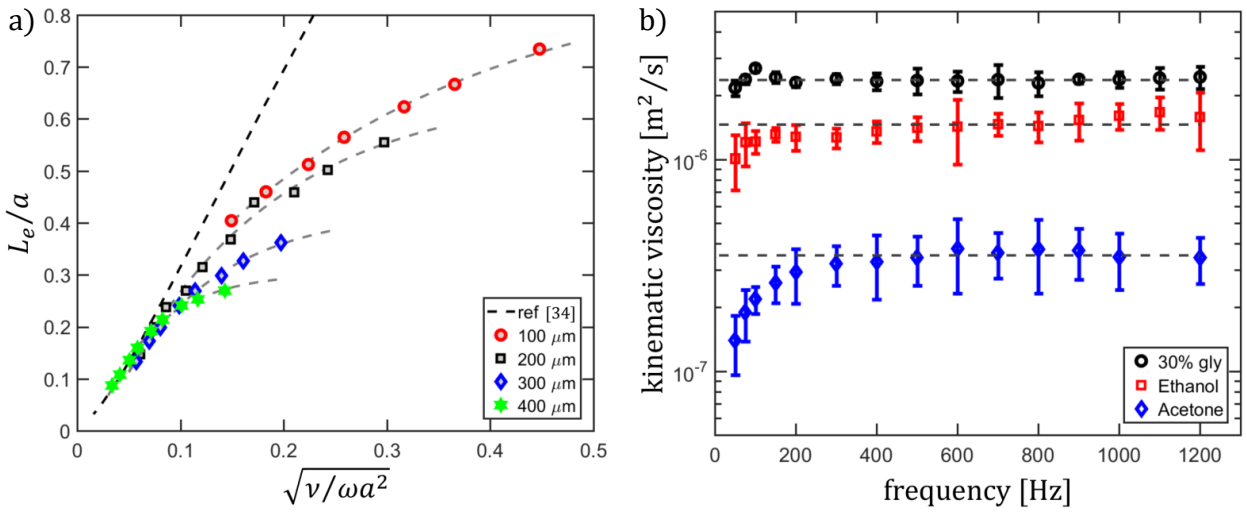

Figure 6.2: (a) Experimental measurements (symbols) of the nondimensional eddy center distance from the cylinder surface versus the nondimensional Stokes boundary layer for water. Calibration curves (grey dashed lines) for each cylinder radius are generated by fitting and exponential function to data points. Experiments converge to the analytical solution [Holtsmark et al., 1954] (black dashed line) at high frequencies and large cylinder radii. (b) Kinematic viscosity measurements of Newtonian liquids using steady streaming flows in microfluidic devices with a cylinder radius of 200 μm. Dashed lines represent that average of individual values for frequencies greater than 300 Hz.

grows very rapidly [Raney et al., 1954]. Eventually, the outer boundary distance becomes greater than the width of the microfluidic channel and, as a result, prevents the eddy center distance from increasing with decreasing frequency.

Since the behavior was consistent for cylinders of different radii, calibration curves were generated by fitting an exponential function, $L_e/a = A - Be^{\sqrt{\nu/\omega a^2}}$, to the experimental data, where A/B is approximately unity (Fig. 6.2 (a), grey dashed lines). Therefore, the kinematic viscosity of a Newtonian liquid can be determined by measuring the location of the dimensionless eddy center for given microfluidic device with cylinder radius a and angular frequency ω. Microfluidic devices with a 200 μm cylinder radius provided the largest dynamic range in measurements of L_e for the range of operation frequencies. Therefore, the 200 μm radius cylinder was utilized for the measurements of the kinematic viscosity of Newtonian liquids.

6.2 Viscometry

The kinematic viscosity of three different Newtonian liquids was determined from the steady streaming profiles in microfluidic devices (Fig. 6.2 (b)) . The Newtonian liquids used were acetone, ethanol, and an aqueous solution of 30% glycerol by weight. Note that while particle tracking methods are not required, tracer particles are still necessary for all measurements to identify the eddy center using the particle pathline visualization method. The sedimentation time for the particles used in ethanol, water, and aqueous 30% glycerol solutions was greater than 24 hours, while for acetone, about half of the particles sediment in $2-3$ hours. Since an experiment for a given frequency in our setup requires only seconds to complete, the sedimentation of particles does not affect the streaming profile. For frequencies greater than 200 Hz, the reported measurements of kinematic viscosity are approximately constant, or independent of oscillation frequency. Therefore, to obtain a single value of the kinematic viscosity, measurements for frequencies of 300 Hz and greater were averaged together.

The average values of kinematic viscosity are represented by grey dashed lines in Figure 6.2 (b). The kinematic viscosity of acetone was measured to be 3.52×10^{-7} m^2/s, which is within 12% of the expected value [Howard and Pike, 1959]. The kinematic viscosity of ethanol was measured to be 1.48×10^{-6} m^2/s, which is within 2.6% of the expected value [Soliman and Marschall, 1990]. Finally, the kinematic viscosity of the 30% glycerol (w/w) solution was measured to be 2.37×10^{-6} m^2/s, which is within 1.6% of the expected value [Glycerine Producers' Association, 1963].

The performance of our technique was compared against tabulated values of kinematic viscosity under similar temperature conditions. The accuracy of our measurements ranged from within 2% to 12% for ethanol and acetone, respectively. The largest discrepancy, in the case of acetone, is attributed to bubble formation within the device. The bubbles originate at the interface between acetone and the electroacoustic transducer due to the volatility of acetone. At lower frequencies, the oscillation amplitudes need to be larger for observable

streaming to occur since streaming velocity scales as $\epsilon^2\omega$. The larger oscillation amplitude therefore results in lower pressures causing greater evaporation and thus stronger bubble formation.

Chapter 7

Viscoelastic liquids in steady streaming flows

The effectiveness of steady streaming as a microrheological tool has been demonstrated above for low-viscosity Newtonian liquids in microfluidic devices [Vishwanathan and Juarez, 2019c]. In this work, we experimentally investigate steady streaming of non-Newtonian liquids in microfluidic devices. A major advantage of the microscale approach is that higher frequencies can be accessed due to lower system inertia arising from small length scales $\mathcal{O}(100\ \mu\text{m})$. Further, smaller cylinder radii enable larger strains and improved spatial-temporal resolution of the rotational inner layer where the liquid rheology is critical, even though comparatively higher frequencies are used. The motivation for our study is three-fold. First, to make quantitative observations on the inner streaming layer of non-Newtonian liquids in the context of microfluidics where they stand to be most likely encountered in contemporary applications. Second, to explore the relationship between the bulk rheology and molecular properties of model dilute and semi-dilute polymer solutions with the observed streaming flows, and third, to elucidate the possible mechanism by which the non-Newtonian behavior manifests in streaming.

7.1 Liquids and rheology

7.1.1 Polymer solutions

Solutions were prepared by step-wise dissolution of different polymers into deionized (DI) water with gentle agitation at 60 rpm for $4-6$ hours. After initial dispersion, the required

final concentration was achieved by successive dilution with DI water. The polymers used in this study were xanthan gum (XG, 2.7×10^6 MW, Sigma Aldrich G1253), non-ionic polyacrylamide (PAA, 6×10^6 MW, Polysciences 02806), and polyacrylamide-acrylate co-polymer with a 30% degree of hydrolysis (hPAA, 18×10^6 MW, Polysciences 18522). In addition to the above aqueous solutions, salinated polyacrylamide-acrylate (hPAAs) was prepared by dissolving hPAA in 0.5 M NaCl solution. The properties of the polymer molecules and the polymer solutions are listed in Table **??**. Estimates of the overlap concentration c^* for these model solutions have been reported in literature [Kulicke and Haas, 1984, Turkoz et al., 2018, François et al., 1979]. Here, all solution concentrations are reported in parts-per-million (ppm) by weight, that is, 1 ppm $= 10^{-6}$ gram of solute per gram of solvent.

7.1.2 Bulk rheology

The steady shear viscosity (η) versus shear rate ($\dot{\gamma}$), and the storage (G') and loss (G'') moduli versus angular frequency (ω) for some polymer solutions are shown in Figure 7.1. We characterize all liquids using a temperature-controlled cone-and-plate geometry rheometer (strain-controlled Ares G2, TA Instruments) at 25 °C. We find strong shear thinning in 1000 ppm xanthan gum (XG 1000) and 50 ppm polyacrylamide-acrylate (hPAA 50) solutions, shown in Figure 7.1 (a). At lower concentration solutions of XG 400 and hPAA 20 (not shown), shear thinning behavior is decreased. Shear thinning is minimal for the 4000 ppm non-ionic polyacrylamide (PAA 4000) and 500 ppm salinated polyacrylamide-acrylate (hPAAs 500) solutions, which can be considered Boger fluids, or constant-viscosity elastic liquids [Boger, 7778, James, 2009].

The steady shear viscosity for the solutions shown in Figure 7.1 (a) are modelled using a Carreau model [Bird et al., 1987], determined by a zero-shear viscosity η_0, infinite-shear viscosity η_∞ (here, assumed to be solvent viscosity), power-law thinning index n and a relaxation time λ_{Cr}. The dynamic moduli of PAA 4000 and hPAAs 500 shown in Figure 7.1 (b) are described well by the Maxwell model [Bird et al., 1987] and characterized by a viscosity η_M,

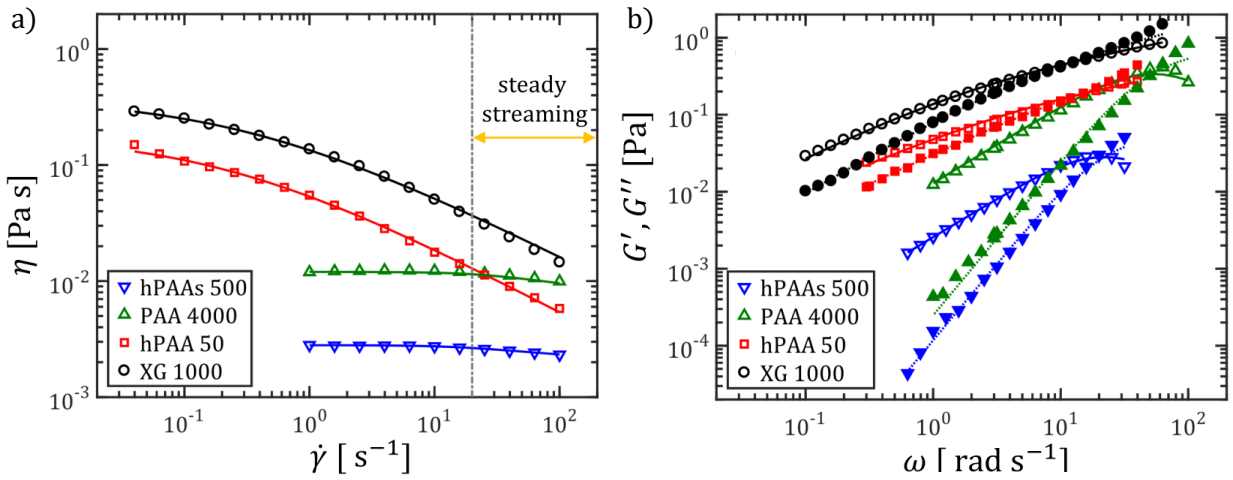

Figure 7.1: (a) Steady state shear viscosity measurements of dilute and semi-dilute polymer solutions used in this study and respective fits (solid line). The yellow arrow shows the mean range of shear rates encountered in experiments. (b) Storage (closed symbols) and loss (open symbols) moduli from oscillatory shear rheology of polymer solutions and model fits shown as solid and dashed lines, respectively. The model parameters used are listed in Table 7.1.

and relaxation time λ_M. The dynamic moduli for XG 1000 and hPAA 50 on the other hand, are modelled well using a fractional Maxwell model (FMM) [Jaishankar and McKinley, 2014] described by two dimensionless exponents: $0 \leq \beta \leq 0.5$ and $\beta \leq \alpha \leq 1$; along with two stiffness quasi-properties $\mathbb{G}$ and $\mathbb{V}$. The model based fits are shown in Figure 7.1 as solid or dashed lines, while the model parameters are listed in Table 7.1.

A relaxation time can also be inferred from the crossover angular frequency (ω_{co}) at which the storage and loss moduli are equal and determined by $\lambda_{co} = 1/\omega_{co}$. A more rigorous estimate of the relaxation time from the model parameters are $\lambda_M \approx \lambda_{co}$ for a Maxwell liquid and $\lambda_{FMM} = (\mathbb{V}/\mathbb{G})^{1/(\alpha-\beta)}$ for a fractional Maxwell liquid. Yet another estimate of the relaxation time for the constant-viscosity polymer solutions (dilute and semi-dilute unentangled) can be obtained from molecular considerations using the Zimm formula [Zimm, 1956]:

$$\lambda_Z = \frac{\eta_s [\eta]_0 M_w}{2.37RT} \ , \tag{7.1}$$

where η_s is the solvent viscosity, $[\eta]_0$ is the intrinsic shear viscosity at zero shear rate, R is the

Table 7.1: Rheological fit parameters used in this study

Carreau	η_0 [Pa s]	η_∞ [Pa s]	λ_{Cr} [s]	n	R^2
hPAA 50	0.119	0.001	4.96	1.51	0.993
XG 1000	0.26	0.001	3.37	1.48	0.988
hPAAs 500	0.0028	0.001	0.074	1.15	0.996
PAA 4000	0.012	0.001	0.046	1.16	0.999
Maxwell	η_M [Pa s]	λ_M [s]			R^2
PAA 4000	0.013	0.019			0.987
hPAAs 500	0.0026	0.046			0.973
FMM	$\mathbb{V}$ [Pa s$^\alpha$]	$\mathbb{G}$ [Pa s$^\beta$]	α	β	R^2
hPAA 50	0.071	0.22	0.75	0.27	0.991
XG 1000	0.23	0.39	0.86	0.34	0.996

The table shows the model parameters used to obtain the fits shown in Figure 7.1. R^2 is a residual quantifying the agreement between the fit and the experimental data.

universal gas constant, and T is the temperature. Here, we take $\eta_s = \eta_\infty = 1 \times 10^{-3}$ Pa s (DI water) and $[\eta]_0$ was approximated for the solutions used based on the zero-shear viscosity and solvent viscosity. The various estimates of relaxation times from the different methods are listed in Table 7.2. Note that the Zimm theory cannot be applied to polyelectrolyte solutions such as XG and hPAA in the absence of salts [Turkoz et al., 2018].

7.2 Qualitative observation

The comparison between steady streaming in Newtonian and non-Newtonian liquids at an oscillation frequency of 600 Hz is shown in Figure 7.2. The particle pathlines (top row) are generated from minimum intensity projections of a sequence of stroboscopic images and the velocity magnitude fields (bottom row) are obtained from particle tracking velocimetry. For all cases, the quadrupolar topology of the streaming flow field is preserved, consisting of four identical vortices with distinct centers. Similarly, the rectified flow moves toward

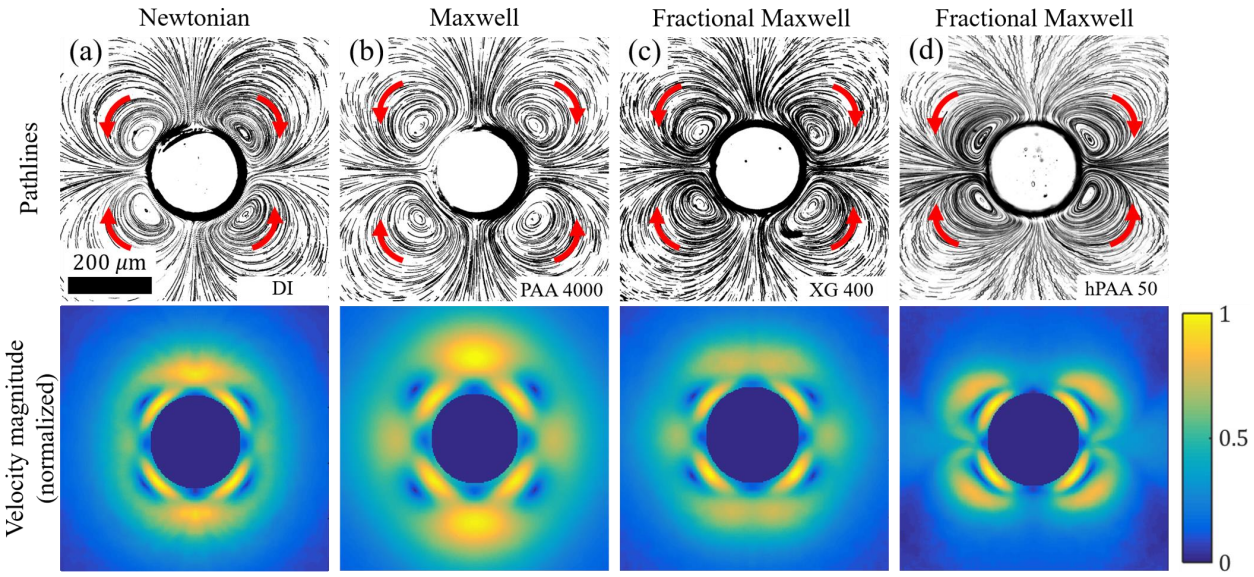

Figure 7.2: Steady streaming profiles in Newtonian and non-Newtonian liquids at an oscillation frequency of 600 Hz around a cylinder with radius of 100 μm. (Top row) Pathlines of tracer particles for (a) DI water and $\epsilon = 0.07$, (b) 4000 ppm non-ionic polyacrylamide and $\epsilon = 0.08$, (c) 400 ppm xanthan gum and $\epsilon = 0.15$, and (d) 50 ppm hydrolyzed polyacrylamide and $\epsilon = 0.19$. (Bottom row) Corresponding steady streaming velocity magnitude field, normalized by the maximum streaming velocity, obtained from particle tracking velocimetry. High-velocity regions, light (or yellow) regions of the colormap, are located near the cylinder boundary.

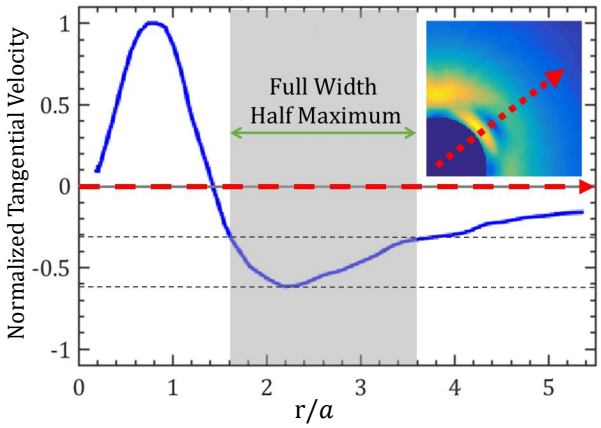

Figure 7.3: Representative steady streaming tangential velocity profile, normalized by the maximum streaming velocity, as a function of dimensionless radial position. This profile is taken along the transect starting from the cylinder surface and radially outward through the eddy center, as shown in the inset. The velocity is highest in magnitude near the cylinder surface and zero at the eddy center location, as it goes from positive to negative values. The full width at half maximum (FWHM) of the second (negative) peak is used to characterize the width of the inner layer and is annotated for DI water at an oscillation frequency of 100 Hz.

the cylinder along the axis of oscillation and away from the cylinder normal to the axis of oscillation.

The pathlines and velocity magnitude field for a Newtonian liquid, deionized water, are shown in Figure 7.2 (a, top and bottom). High flow velocities are located in the regions between the cylinder surface and the eddy center, and near the cylinder surface, perpendicular to the axis of oscillation. This latter difference, compared to the velocity along the axis, is because of increased interaction with the channel wall in the breadthwise direction as compared to the lengthwise direction.

The steady streaming pathlines and velocity magnitude field of a Maxwell liquid, PAA 4000, are qualitatively similar to that of a Newtonian liquid, shown in Figure 7.2 (b, top and bottom). The main difference, compared with DI water, is the eddy center distance from the cylinder surface, which is larger for PAA 4000. This larger eddy center distance indicates a higher viscosity for PAA 4000, as was recently demonstrated [Vishwanathan and Juarez, 2019c], and is in agreement with steady state shear viscosity measurements shown in Figure 7.1 (a).

In the fractional Maxwell liquids, a qualitative difference is observed in particle pathlines and velocity magnitude fields. For XG 400 solutions, the angular position of the eddy centers move closer to the axis of oscillation, shown in Figure 7.2 (c, top). The velocity field has also observably changed with the velocity maximum, normal to the axis of oscillation, separated into two regions by a local minimum, shown in Figure 7.2 (c, bottom). For hPAA 50 solutions, a more prominent change is seen where the angular position of the eddy center as well as the velocity maximum are moved considerably towards the axis of oscillation, Figure 7.2 (d, top and bottom).

7.3 Velocity field results

To quantify differences in the steady streaming profile for various liquids over a range of frequencies, the normalized tangential velocity profile as a function of the dimensionless radial position (r/a) along a transect from the cylinder surface through the eddy center was examined. The transect is depicted by the red dashed arrow passing through the eddy center in Figure 7.3 (inset). A representative experimentally measured velocity profile for a Newtonian liquid is shown in Figure 7.3. The particular parameter of interest is the full width at half maximum (FWHM) of the second peak, beyond the eddy center. The FWHM provides a measure of the size of the inner layer in this streaming regime where a distinctly visible separation between the inner and outer layers is absent. The FWHM is also preferred because of the insensitivity to inaccuracies in particle tracking close to the cylinder surface as well as inaccuracies in the measurement of oscillation amplitude (s).

The variation of the FWHM with frequency for Newtonian liquids, DI water and aqueous 60% glycerol (w/w) with a dynamic viscosity of 5.9 mPa s, and Maxwell liquids, PAA 4000 and hPAAs 500, is shown in Figure 7.4 (a). The Newtonian liquids exhibit slow monotonic decrease in the FWHM with increasing oscillation frequency. The Maxwell liquids show a nominally faster rate of decrease in the FWHM with increasing frequency, without any

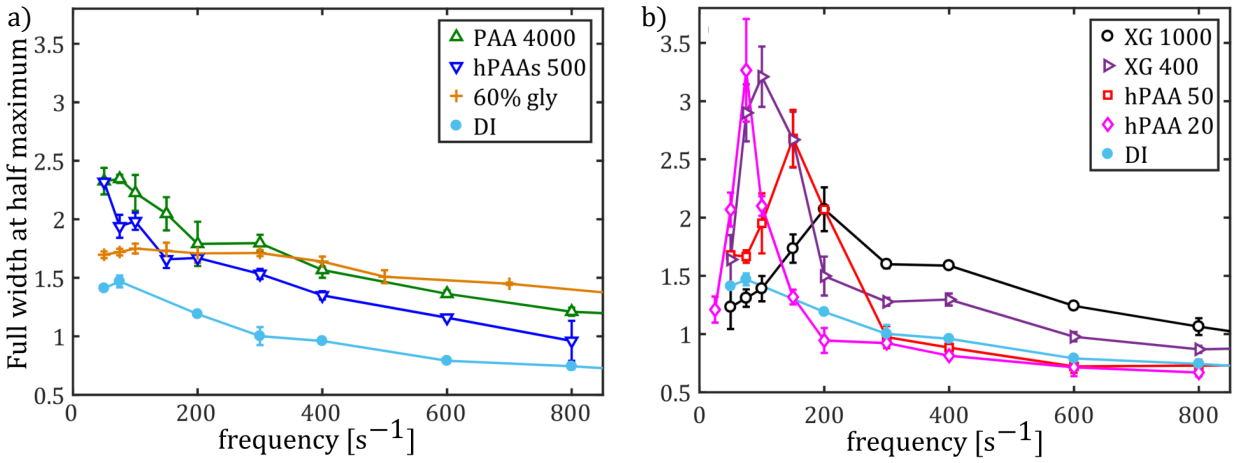

Figure 7.4: Evolution of inner streaming layer characterized by the full width at half maximum for Newtonian and non-Newtonian liquids as a function of oscillation frequency in microfluidic devices. (a) The FWHM of Newtonian liquids and Maxwell liquids exhibit monotonic decrease with increasing oscillation frequency. (b) The FWHM of fractional Maxwell liquids, however, increases to a maximum value and then decreases with increasing oscillation frequency.

discernible features.

This is in sharp contrast with the observations for fractional Maxwell liquids. All four polymer solutions exhibit distinct peaks in their FWHM with increasing oscillation frequency, shown in Figure 7.4 (b). For hPAA 50 ppm solutions, the FWHM grows rapidly for oscillation frequencies of 75 Hz to 150 Hz, which is in agreement with previous observations [Vlassopoulos and Schowalter, 1993]. However, the FWHM begins to decrease with further increasing frequency until its variation is similar to that of the solvent. Similar trends are observed for hPAA 20 solutions, with the maximum FWHM observed at 75 Hz and a subsequent rapid decrease to Newtonian-like behavior.

The XG 1000 and XG 400 solutions also behave in a manner consistent with our observations for the hPAA solutions, exhibiting a distinct peak in the FWHM followed by a decrease to Newtonian-like behavior with increasing frequency. The key difference between the two polymers is the rate at which they decrease at large frequencies, which is slower for XG solutions. This is in agreement with the qualitative observations where the pathlines and the corresponding velocity magnitude fields are not as distorted in XG as they are in

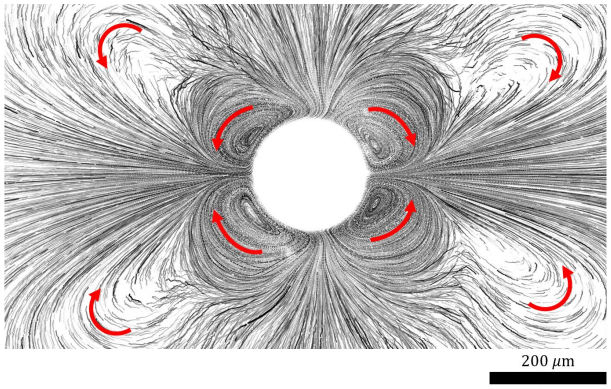

Figure 7.5: Pathlines of tracer particles illustrating experimental evidence of the predicted cascading inertio-elastic vortices. A set of secondary, same-sense vortices is shown for an hPAA 50 polymer solution at an oscillation frequency of 800 Hz and non-dimensional amplitude of $\epsilon = 0.2$.

hPAA, even at 600 Hz, shown in Figure 7.2 (c) and (d). Further increase in frequency is not found to significantly alter the velocity profile of hPAA 20 and hPAA 50 solutions, while XG 400 shows a gradual approach towards velocity fields similar to those of hPAA 50. This approach is slower still for XG 1000 and therefore reflected completely by the evolution of the FWHM shown in Figure 7.4.

7.4 Interpretation

The significant departure from four-fold symmetry in the streaming flow profile observed for Fractional Maxwell liquids, as compared to the Newtonian case in Figure 3.1(top), is attributed to the nature of the oscillatory strain field and the shear thinning rheology of these liquids (see Figure 2.1 (a)). At leading order, the rate of strain ($\mathcal{O}(\epsilon\omega)$) in the vicinity of the cylinder is completely extensional along the axis of oscillation, and purely shearing perpendicular to it. The spatial-temporal mean rates of extension and shear obtained theoretically [Holtsmark et al., 1954] for DI water with $\nu = 10^{-6}$ m^2/s and a cylinder radius of 100 μm are $0.15\epsilon\omega$ and $0.45\epsilon\omega$, respectively. For the frequencies used in this study, the mean strain rates are in the range $50 - 200$ s^{-1} for shear (shown in Figure 2.1 (a)) and $15 - 60$ s^{-1}

in the case of extension. The corresponding maximum, instantaneous rates of extension and shear are $0.3\epsilon\omega$ and $3.73\epsilon\omega$, respectively. The relatively large prefactor for shear is due to its localization near the cylinder surface. As a result, the effective viscosity is considerably lower in the high shear region for liquids exhibiting shear thinning, and consequently asymmetry is observed in the streaming flow profile. Maxwell liquids, on the other hand, exhibit minimal shear thinning behavior in this range of shear rates. Therefore, the location of the eddy center and overall streaming flow profile does not differ significantly in comparison to Newtonian liquids.

The growth of the inner streaming layer for a cylinder oscillating at frequencies $f <$ 100 Hz in dilute hydrolyzed polyacrlyamide solutions has been experimentally observed [Vlassopoulos and Schowalter, 1993]. Although the growth of the inner layer at unity Deborah numbers (De$= \lambda\omega \approx 1$) was analytically understood to be an effect of elasticity using viscoelastic models [Frater, 1967, James, 1977, Chang, 1977], the most relevant estimate of the relaxation time remains ambiguous. Different estimates of relaxation time for liquids such as hPAA 50 and XG 1000 that show inner layer growth, are listed in Table 7.2. The estimates vary considerably depending on the rheology data used, all of which yield De$>$ 10, even at 20 Hz.

In contrast, the experimental results presented here for Maxwell liquids indicate a decrease of the inner layer width, without the characteristic growth. While this observation is consistent with previous experiments, which report almost Newtonian behavior for similar liquids [Vlassopoulos and Schowalter, 1993], we note that De$>$ 10 even at 100 Hz, regardless of the relaxation time estimate used from Table 3.2. This lack of inner layer growth is unsurprising when we consider that coil-stretch transitions are theorized to require $\dot{\varepsilon}\lambda_Z > 1$ in purely extensional flow [de Gennes, 1974, Larson and Magda, 1989]. Estimating the maximum instantaneous rate of extension in our experiments ($\dot{\varepsilon} \leq 0.3\epsilon\omega$) to be $30 - 100$ s^{-1}, the values of λ_Z shown in Table 7.2 do not satisfy the criterion. Hence, polymer stretching in the primary flow is likely insufficient for the growth of the inner streaming layer in Maxwell

liquids.

The decrease of the inner layer width following the initial growth in the fractional Maxwell liquids has not been reported before and is best explained by a competition between the effects of inertia and elasticity. This competition was suggested in the theoretical analysis for an oscillating sphere (see Fig. 4 and Fig. 6 in Ref. [Böhme, 1992]) and quantified through the material functions $S = \rho a^2\omega^2/G''$ and $V = G'/G''$, which are analogs of the Reynolds number and Deborah number, respectively. Similar to theories for a cylinder, increasing V while keeping S fixed was found to increase the width of the inner streaming layer. Increasing S for a fixed V, however, results in a set of cascading same sense vortices, of which, the innermost vortex decreases in width. Owing to the dependence of both S and V on ω, it is difficult to experimentally achieve independent control.

Regardless, the first experimental evidence of cascading same sense vortices for a fractional Maxwell liquid (hPAA 50) at 800 Hz is shown in Figure 5.1. An important implication of this observation is that, eventually, the effect of a growing S dominates over that of a growing V. Indeed, we find that this is the case from Figure 7.6 which shows the variation of the material functions S and V with frequency for the models and fit parameters given in Table 7.1. The values to the left of the vertical dotted line lie in the range of frequencies for which the oscillatory rheology was measured while those to the right are an extrapolation and lie in the frequency range for which streaming is studied.

For fractional Maxwell liquids (dotted lines) and frequencies $f > 100$ Hz, V saturates in the range of $1.5 < V < 2$ while S grows much faster to $10 < S < 100$. Therefore, there is quantitative concord with our experimental observations of growth and subsequent shrinking of the inner layer beyond $(V = 1.5, S = 50)$, and the corresponding values of $(V = 2, S = 50)$ shown elsewhere [Böhme, 1992] at which the cascading vortices manifest, albeit for a sphere. This suggests that a description of viscoelasticity in terms of S and V is more robust than one based on relaxation times.

For the Maxwell liquids, however, the material function V increases rapidly when ex-

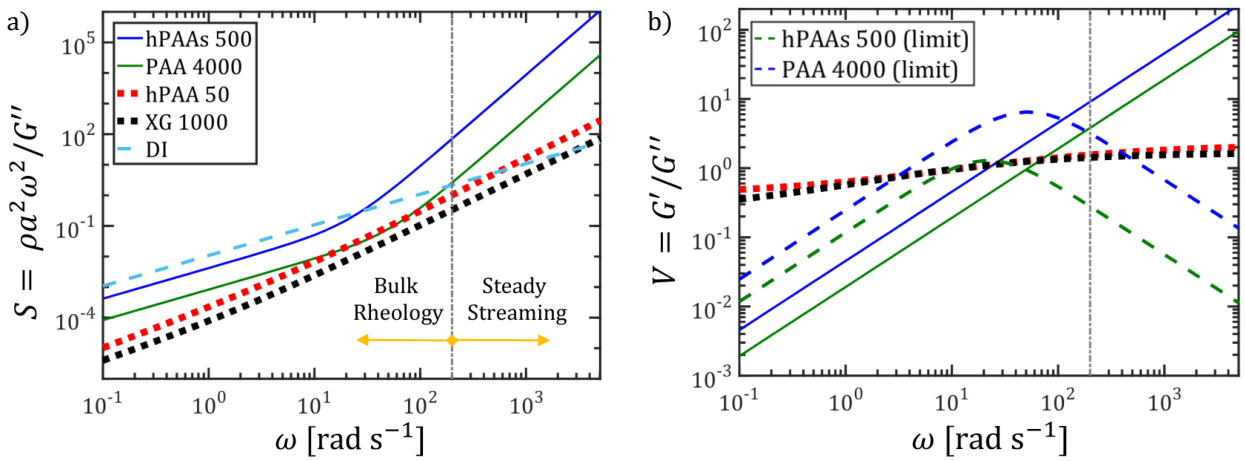

Figure 7.6: Variation of S (top) and V (bottom) with angular frequency based on the rheology fit models. Oscillatory rheology was performed in the frequency range to the left of the vertical line while streaming experiments were performed in the range of frequencies to the right.

trapolated to frequencies $f > 20$ Hz (solid lines in Figure 7.6 (b). Notwithstanding that the polymer chains are likely insufficiently stretched in the flow, it is worth noting that rapid growth of V for a Maxwell liquid is unphysical because it requires an indefinitely decreasing G'' for an approximately constant G'. The solvent viscosity (here $\eta_\infty = 1$ mPa.s) provides a definite lower bound on the loss modulus, and hence, an upper bound for V given by $G'/(\eta_\infty \omega)$ and shown in Figure 7.6 ((b), dashed lines). Thus, for the Maxwell liquids, an increasing ω will eventually lead to a decrease in V or, at least, a significant decrease in its growth with frequency. This is also true of S for which is limited by the corresponding curve for DI water (top, dashed lines).

Table 7.2: Relaxation time estimates from different models

Polymer solution	λ_Z [ms]	λ_{co} [ms]	λ_{Cr} [ms]	λ_{FMM} [ms]
XG 1000	-	79	3370	362
PAA 4000	2.7	17	46	-
hPAA 50	-	83	4960	94.7
hPAAs 500	11.2	50	74	-

Above, λ_Z is from Zimm theory, λ_{co} is from the crossover of dynamic moduli, λ_{Cr} is from the Carreau model, and λ_{FMM} is from the fractional Maxwell model. The relaxation times may be compared to $\lambda_{ref} = 0.4$ ms, for which $\lambda_{ref}\omega = 1$ at 400 Hz.

Chapter 8

Concluding remarks

We have discussed an accessible, effective, and versatile plug and play technique to generate oscillatory flows over a range of amplitudes and frequencies in microchannels. By directly interfacing microfluidic tubing with a loudspeaker diaphragm, sub-kilohertz oscillatory flows in the range of $10-1000$ Hz with amplitudes in the range of $10-600$ μm are produced. The corresponding wavelengths lie between $1-100$ m and are far larger than the dimensions of a typical microchannel. Thus, nearly unattenuated flows of a uniform phase can be achieved throughout. This is in contrast with flows in the $10^4 - 10^7$ Hz range where attenuation is significant and effects are usually local to the transducer. The resulting velocity profiles can also be tuned from Stokes-like flow ($W/\delta \leq 4$) at low frequencies to plug-like unsteady Stokes flow ($W/\delta \geq 7.5$) at high frequencies allowing for manipulation of the flow profile for a given micro-scale geometry. In addition to coherent oscillatory flows, strong and well defined rectified flows near curved boundaries and interfaces are also made possible in this frequency and amplitude range.

The guiding principles for applications are two-fold. First, oscillatory flows permit an increase the net distance travelled by the fluid without an accompanied increase in flow rate, shear rate, pressure drop, or particle displacement seen in long channel steady flows and high throughput applications. More generally, such conditions are particularly useful when the desired sample or analyte response to the flow environment is directionally invariant. In theory, the resulting effect can be increased indefinitely by simply increasing the frequency of oscillation. Although in practice, attenuation and secondary flows which grow stronger with increasing frequency prevent this from being realized. Owing to the large wavelengths in this

range of flows, attenuation is limited while secondary flows usually become significant only for frequencies larger than 100 Hz implying that an optimum frequency is likely encountered in the range of frequencies realized here. The resulting lower steady pressure drop and steady shear rates are particularly useful for cells and other suspended biological matter that are sensitive to or potentially damaged by prolonged exposure to excessive shear rates or pressures. The absence of particle net displacement is useful in decreasing the footprint of microfluidic devices and in situations where continuous observation is needed to track the evolution in processes such as cell growth or chemical synthesis in dynamic environments.

Second, the steady rectified flow speeds are of considerable magnitude despite the maximum frequency considered being much smaller than the typical resonant frequencies of piezoelectric transducers ($1 - 100$ kHz). This is because of the large amplitudes accessed by the loudspeaker diaphragm and the dependency of flow speed on amplitude, which scales as $s^2\omega$. Further, the Stokes boundary layer thickness is accurately controlled and varies in size from $10 \leq \delta \leq 100$ μm for the highest and lowest frequencies accessed here, respectively. Therefore, the flow pathlines are less sensitive to manufacturing defects and feature surface quality, making this approach more amenable to precision applications such as sorting, trapping and manipulation of particles and cells, and other controlled mass transfer applications.

Additionally the steady secondary flows around a solid PDMS cylinder referred to more commonly as steady streaming has been used to measure the kinematic viscosity of low volume ($<$0.1 ml) and low viscosity ($<$10 cP) Newtonian liquids in a relatively quick (1-10 s) probe-free and entirely visual manner.

The applicability of steady streaming in measuring the rheology of viscoelastic liquids has been critically examined. The potential advantages of using steady streaming for characterizing viscoelastic solutions include the ability to create large strains due to small length scales and access frequencies larger than those accessible in conventional rheometry. Steady streaming presents an additional advantage where a well defined De is distinctly known since

monotone frequencies are used. The inner steady streaming layer of dilute and semi-dilute polymer solutions, having both Maxwell and fractional Maxwell oscillatory shear rheology. Qualitative differences in the velocity fields are observed for fractional Maxwell liquids, most prominently, an angular displacement of the eddy centers towards the direction of oscillation and consequent asymmetry. The inner streaming layer width characterized by FWHM of fractional Maxwell liquids exhibits a non-monotonic relationship with oscillation frequency; first increasing in width followed by a decrease in width with increasing frequency. This behavior is attributed to a competition between elasticity and inertia, with inertia dominating at high frequencies. Maxwell liquids, however, exhibit a monotonic decrease of the inner streaming layer width with increasing frequency at a rate nominally faster than that observed for a Newtonian liquid. Even for oscillation periods considerably smaller than the molecular relaxation time, we do not observe any qualitative change in the flow profile as compared to a Newtonian liquid. This behavior is attributed to the insufficient molecular stretching by the underlying oscillatory flow.

References

[Abolhasani and Jensen, 2016] Abolhasani, M. and Jensen, K. F. (2016). Oscillatory multiphase flow strategy for chemistry and biology. *Lab on a Chip*, 16:2775–2784.

[Ahmed et al., 2009] Ahmed, D., Mao, X., Shi, J., Juluri, B. K., and Huang, T. J. (2009). A millisecond micromixer via single-bubble-based acoustic streaming. *Lab on Chip*, 9:2738–2741.

[Alizadehgiashi et al., 2009] Alizadehgiashi, M., Khabibullin, A., Li, Y., Prince, E., Abolhasani, M., and Kumacheva, E. (2009). Shear-induced alignment of anisotropic nanoparticles in a single-droplet oscillatory microfluidic platform. *Lab on a Chip*, 9:2738–2741.

[Amini et al., 2012] Amini, H., Sollier, E., Weaver, W. M., and Carlo, D. D. (2012). Intrinsic particle-induced lateral transport in microchannels. *Proceedings of the National Academy of Sciences*, 109:11593–11598.

[Amit et al., 2016] Amit, R., Abadi, A., and Kosa, G. (2016). Characterization of steady streaming for a particle manipulation system. *Biomedical Microdevices*, 18:39.

[Bachman et al., 2019] Bachman, H., Fu, H., hsun Huang, P., Tian, Z., Embry-Seckler, J., Rufo, J., Xie, Z., Hartman, J. H., Zhao, S., Yang, S., Meyer, J. N., and Huang, T. J. (2019). Open source acoustofluidics. *Lab on a Chip*, 19:2404–2414.

[Basilio et al., 2019] Basilio, P. A., Torres Rojas, A. M., Corvera Poiré, E., and Olguín, L. F. (2019). Stream of droplets as an actuator for oscillatory flows in microfluidics. *Microfluidics and Nanofluidics*, 23(5):64.

[Bhagat et al., 2010] Bhagat, A. A. S., Kuntaegowdanahalli, S. S., Kaval, N., Seliskar, C. J., and Papautsky, I. (2010). Inertial microfluidics for sheath-less high-throughput flow cytometry. *Biomedical Microdevices*, 12:187–195.

[Bird et al., 1987] Bird, R. B., Armstrong, R. C., and Hassager, O. (1987). *Dynamics of Polymeric Liquids. Vol. 1, 2nd Ed.: Fluid Mechanics*. Wiley.

[Boger, 7778] Boger, D. V. (1977/78). A highly elastic constant-viscosity fluid. *Journal of Non-Newtonian Fluid Mechanics*, 3:87–91.

[Böhme, 1992] Böhme, G. (1992). On streaming in viscoelastic liquids. *Journal of Non-Newtonian Fluid Mechanics*, 44:149–170.

[Cai et al., 2017] Cai, G., Xue, L., Zhang, H., and Lin, J. (2017). A review on micromixers. *Micromachines*, 8:274.

[Chang, 1977] Chang, C. (1977). Boundary layer analysis of oscillating cylinder flows in a viscoelastic liquid. *Journal of Applied Mathematics and Physics*, 28:283–288.

[Chang and Schowalter, 1974] Chang, C. and Schowalter, W. R. (1974). Flow near and oscillating cylinder in dilute viscoelastic fluid. *Nature*, 252:686–688.

[Chang and Schowalter, 1979] Chang, C. and Schowalter, W. R. (1979). Secondary flow in the neighborhood of a cylinder oscillating in a viscoelastic fluid. *Journal of Non-Newtonian Fluid Mechanics*, 6:47–67.

[Chong et al., 2013] Chong, K., Kelly, S. D., Smith, S., and Eldredge, J. (2013). Inertial particle trapping in viscous streaming. *Physics of Fluids*, 25:033602.

[Coenen, 2016] Coenen, W. (2016). Steady streaming around a cylinder pair. *Proceedings of the Royal Society A*, 472:20160522.

[de Gennes, 1974] de Gennes, P. G. (1974). Coil[U+2010]stretch transition of dilute flexible polymers under ultrahigh velocity gradients. *The Journal of Chemical Physics*, 60(12):5030–5042.

[Di Carlo, 2009] Di Carlo, D. (2009). Inertial microfluidics. *Lab on a Chip*, 9:3038–3046.

[Di Carlo et al., 2007] Di Carlo, D., Irimia, D., Tompkins, R. G., and Toner, M. (2007). Continuous inertial focusing, ordering, and separation of particles in microchannels. *Proceedings of the National Academy of Sciences*, 104:18892–18897.

[François et al., 1979] François, J., Sarazin, D., Schwartz, T., and Weill, G. (1979). Polyacrylamide in water: molecular weight dependence of $\langle R^2 \rangle$ and $[\eta]$ and the problem of the excluded volume exponent. *Polymer*, 20(8):969 – 975.

[Frater, 1967] Frater, K. R. (1967). Acoustic streaming in an elastico-viscous fluid. *Journal of Fluid Mechanics*, 30(4):689–697.

[Friend and Yeo, 2011] Friend, J. and Yeo, L. Y. (2011). Microscale acoustofluidics: Microfluidics driven via acoustics and ultrasonics. *Reviews of Modern Physics*, 83:647–704.

[Frommelt et al., 2008] Frommelt, T., Kostur, M., Wenzel-Schäfer, M., Talkner, P., Hänggi, P., and Wixforth, A. (2008). Microfluidic mixing via acoustically driven chaotic advection. *Phys. Rev. Lett.*, 100:034502.

[Galindo-Rosales and Alves, 2013] Galindo-Rosales, F. J. and Alves, M. A. (2013). Microdevices for extensional rheometry of low viscosity elastic liquids: A review. *Microfluidics and Nanofluidics*, 14:1–19.

[Girardo et al., 2008] Girardo, S., Cecchini, M., Beltram, F., Cingolani, R., and Pisignano, D. (2008). Polydimethylsiloxane-$LiNbO_3$ surface acoustic wave micropump devices for fluid control into microchannels. *Lab on a Chip*, 8:1557–1563.

[Giudice et al., 2015] Giudice, F. D., D'Avino, G., Greco, F., Santo, I. D., Netti, P. A., and Maffettone, P. L. (2015). Rheometry-on-a-chip: measuring the relaxation time of a viscoelastic liquid through particle migration in microchannel flows. *Lab on a Chip*, 15:783.

[Giudice et al., 2017a] Giudice, F. D., Haward, S. J., and Shen, A. Q. (2017a). Relaxation time of dilute polymer solutions: A microfluidic approach. *Journal of Rheology*, 61:327.

[Giudice et al., 2017b] Giudice, F. D., Tassieri, M., Oelschlaeger, C., and Shen, A. Q. (2017b). When microrheology, bulk rheology, and microfluidics meet: Broadband rheology of hydroxyethyl cellulose water solutions. *Macromolecules*, 50:2951–2963.

[Glycerine Producers' Association, 1963] Glycerine Producers' Association (1963). *Physical properties of glycerine and its solutions*. Glycerine Producers' Association, New York.

[Groisman et al., 2003] Groisman, A., Enzelberger, M., and Quake, S. R. (2003). Microfluidic memory and control devices. *Science*, 300(5621):955–958.

[Gupta et al., 2016] Gupta, S., Wang, W. S., and Vanapalli, S. A. (2016). Microfluidic viscometers for shear rheology of complex fluids and biofluids. *Biomicrofluidics*, 10:043402.

[Haward, 2016] Haward, S. J. (2016). Microfluidic extensional rheometry using stagnation point flow. *Biomicrofluidics*, 10:043401.

[Hessel et al., 2005] Hessel, V., Löwe, H., and Schönfeld, F. (2005). Micromixers - a review on passive and active mixing principles. *Chemical Engineering Science*, 60:2479–2501.

[Holtsmark et al., 1954] Holtsmark, J., Johnsen, I., Sikkeland, T., and Skavlem, S. (1954). Boundary layer flow near a cylindrical obstacle in an oscillating, incompressible fluid. *The Journal of the Acoustical Society of America*, 26:26.

[Howard and Pike, 1959] Howard, K. S. and Pike, F. P. (1959). Viscosities and densities of acetone-benzene and acetone-acetic acid systems up to their normal boiling points. *Journal of Chemical and Engineering Data*, 4:331–333.

[Hur et al., 2010] Hur, S. C., Tse, H. T. K., and Carlo, D. D. (2010). Sheathless inertial cell ordering for extreme throughput flow cytometry. *Lab on a Chip*, 10:274–280.

[Jaishankar and McKinley, 2014] Jaishankar, A. and McKinley, G. H. (2014). A fractional K-BKZ constitutive formulation for describing the nonlinear rheology of multiscale complex fluids. *Journal of Rheology*, 58:1751–1788.

[James, 2009] James, D. F. (2009). Boger fluids. *Annual Review of Fluid Mechanics*, 41:129–142.

[James, 1977] James, P. W. (1977). Elastico-viscous flow around a circular cylinder executing small amplitude, high frequency oscillations. *Journal of Non-Newtonian Fluid Mechanics*, 2:99–107.

[Jo et al., 2009] Jo, K., Chen, Y.-L., de Pablo, J. J., and Schwartz, D. C. (2009). Elongation and migration of single dna molecules in microchannels using oscillatory shear flows. *Lab on a Chip*, 9:2348–2355.

[Kim et al., 2013] Kim, S. J., Yokokawa, R., and Takayama, S. (2013). Microfluidic oscillators with widely tunable periods. *Lab on a Chip*, 13:1644–1648.

[Kulicke and Haas, 1984] Kulicke, W. M. and Haas, R. (1984). Flow behavior of dilute polyacrylamide solutions through porous media. 1. influence of chain length, concentration, and thermodynamic quality of the solvent. *Industrial & Engineering Chemistry Fundamentals*, 23(3):308–315.

[Kuntaegowdanahalli et al., 2009] Kuntaegowdanahalli, S. S., Bhagat, A. A. S., Kumar, G., and Papautsky, I. (2009). Inertial microfluidics for continuous particle separation in spiral microchannels. *Lab on a Chip*, 9:2973–2980.

[Landau and Lifshits, 1959] Landau, L. D. and Lifshits, E. M. (1959). *Fluid Mechanics, Translated by J.B. Sykes and W.H. Reid.*, volume 6 of *Course of theoretical physics*. Pergamon Press: London.

[Larson and Magda, 1989] Larson, R. G. and Magda, J. J. (1989). Coil-stretch transitions in mixed shear and extensional flows of dilute polymer solutions. *Macromolecules*, 22:3004–3010.

[Lee et al., 2011] Lee, C. Y., Chang, C. L., Wang, Y. N., and Fu, L. M. (2011). Microfluidic mixing: A review. *International Journal of Molecular Sciences*, 12:3263–3287.

[Lee et al., 2016] Lee, C. Y., Wang, W. T., Chang, C. L., and Fu, L. M. (2016). Passive mixers in microfluidic systems: A review. *Chemical Engineering Journal*, 288:146–160.

[Leslie et al., 2009] Leslie, D. C., Easley, C. J., Seker, E., Karlinsey, J. M., Utz, M., Begley, M. R., and Landers, J. P. (2009). Frequency-specific flow control in microfluidic circuits with passive elastomeric features. *Nature Physics*, 5:231–235.

[Lestari et al., 2016] Lestari, G., Salari, A., Abolhasani, M., and Kumacheva, E. (2016). A microfluidic study of liquid–liquid extraction mediated by carbon dioxide. *Lab on a Chip*, 16:2710–2718.

[Lieu et al., 2012] Lieu, V. H., House, T. A., and Schwartz, D. T. (2012). Hydrodynamic tweezers: Impact of design geometry on flow and microparticle trapping. *Analytical Chemistry*, 84.

[Liu et al., 2000] Liu, R. H., Stremler, M. A., Sharp, K. V., Olsen, M. G., Santiago, J. G., Adrian, R. J., Aref, H., and Beebe, D. J. (2000). Passive mixing in a three-dimensional serpentine microchannel. *Journal of Microelectromechanical Systems*, 9:190–197.

[Liu et al., 2002] Liu, R. H., Yang, J., Pindera, M. Z., Athavale, M., and Grodzinski, P. (2002). Bubble-induced acoustic micromixing. *Lab on a Chip*, 2:151–157.

[Lutz et al., 2006a] Lutz, B. R., Chen, J., and D. T. Schwartz, D. (2006a). Hydrodynamic tweezers: 1. noncontact trapping of single cells using steady streaming microeddies. *Analytical Chemistry*, 78:5429–5435.

[Lutz et al., 2006b] Lutz, B. R., Chen, J., and Schwartz, D. T. (2006b). Characterizing homogeneous chemistry using well-mixed microeddies. *Analytical Chemistry*, 78:1606–1612.

[Marmottant and Hilgenfeldt, 2003] Marmottant, P. and Hilgenfeldt, S. (2003). Controlled vesicle deformation and lysis by single oscillating bubbles. *Nature*, 423:153–156.

[Martel and Toner, 2014] Martel, J. M. and Toner, M. (2014). Inertial focusing in microfluidics. *Annual Review of Biomedical Engineering*, 16:371–396.

[Morris and Forster, 2000] Morris, C. J. and Forster, F. K. (2000). The correct treatment of harmonic pressure-flow behavior in microchannels. *Micro-Electro-Mechanical Systems*, pages 473–479.

[Mosadegh et al., 2010] Mosadegh, B., Kuo, C. H., Tung, Y. C., Torisawa, Y. S., Bersano-Begey, T., Tavana, H., and Takayama, S. (2010). Integrated elastomeric components for autonomous regulation of sequential and oscillatory flow switching in microfluidic devices. *Nature Physics*, 6:433–437.

[Mutlu et al., 2018] Mutlu, B. R., Edd, J. F., and Toner, M. (2018). Oscillatory inertial focusing in infinite microchannels. *Proceedings of the National Academy of Sciences*, 115:7682–7687.

[Nguyen and Wu, 2005] Nguyen, N. T. and Wu, Z. (2005). Micromixers - a review. *Journal of Micromechanics and Microengineering*, 15:R1–R16.

[Nivedita and Papautsky, 2013] Nivedita, N. and Papautsky, I. (2013). Continuous separation of blood cells in spiral microfluidic devices. *Biomicrofluidics*, 7:054101.

[Oakey et al., 2010] Oakey, J., Applegate, R. W., Arellano, E., Carlo, D. D., Graves, S. W., and Toner, M. (2010). Particle focusing in staged inertial microfluidic devices for flow cytometry. *Analytical Chemistry*, 82:3862–3867.

[Ober et al., 2015] Ober, T. J., Foresti, D., and Lewis, J. A. (2015). Active mixing of complex fluids at the microscale. *Proceedings of the National Academy of Sciences*, 112:12293–12298.

[O'Brien, 1975] O'Brien, V. (1975). Pulsatile fully developed flow in rectangular channels. *Journal of the Franklin Institute*, 300:225 – 230.

[Ottino and Wiggins, 2004] Ottino, J. M. and Wiggins, S. (2004). Introduction: Mixing in microfluidics. *Philosophical Transactions of the Royal Society A*, 362:923–935.

[Ouellette et al., 2006] Ouellette, N. T., Xu, H., and Bodenschatz, E. (2006). A quantitative study of three-dimensional Lagrangian particle tracking algorithms. *Experiments in Fluids*, 40:301–313.

[Phelan et al., 2008] Phelan, F. R., Hughes, N. R., and Pathak, J. A. (2008). Chaotic mixing in microfluidic devices driven by oscillatory cross flow. *Physics of Fluids*, 20(2):023101.

[Phillips et al., 2016] Phillips, R. H., Jain, R., Browning, Y., Shah, R., Kauffman, P., Dinh, D., and Lutz, B. R. (2016). Flow control using audio tones in resonant microfluidic networks: towards cell-phone controlled lab-on-a-chip devices. *Lab on a Chip*, 16:3260–3267.

[Pipe and McKinley, 2009] Pipe, C. J. and McKinley, G. H. (2009). Microfluidic rheometry. *Mechanics Research Communications*, 36:110–120.

[Qu et al., 2017] Qu, J., Wu, H., Cheng, P., Wang, Q., and Sun, Q. (2017). Recent advances in mems-based micro heat pipes. *International Journal of Heat and Mass Transfer*, 110:294 – 313.

[Rallabandi et al., 2017] Rallabandi, B., Wang, C., and Hilgenfeldt, S. (2017). Analysis of optimal mixing in open-flow mixers with time-modulated vortex arrays. *Physical Review Fluids*, 2:064501.

[Raney et al., 1954] Raney, W. P., Corelli, J. C., and Westervelt, P. J. (1954). Acoustical streaming in the vicinity of a cylinder. *The Journal of the Acoustical Society of America*, 26:1006–1014.

[Riley, 2001] Riley, N. (2001). Steady streaming. *Annual Review of Fluid Mechanics*, 33:43–65.

[Schmid et al., 2014] Schmid, L., Weitz, D. A., and Franke, T. (2014). Sorting drops and cells with acoustics: acoustic microfluidic fluorescence-activated cell sorter. *Lab on a Chip*, 14:3710–3718.

[Seo et al., 2007] Seo, J., Lean, M. H., and Kole, A. (2007). Membrane-free microfiltration by asymmetric inertial migration. *Applied Physics Letters*, 91:033901.

[Shmilovitz, 2005] Shmilovitz, D. (2005). On the definition of total harmonic distortion and its effect on measurement interpretation. *IEEE Transactions on Power Delivery*, 20(1):526–528.

[Soliman and Marschall, 1990] Soliman, K. and Marschall, E. (1990). Viscosity of selected binary, ternary, and quaternary liquid mixtures. *Journal of Chemical and Engineering Data*, 35:375–381.

[Squires and Mason, 2010] Squires, T. M. and Mason, G. (2010). Fluid mechanics of microrheology. *Annual Review of Fluid Mechanics*, 42:413–438.

[Sritharan et al., 2006] Sritharan, K., Strobl, C. J., Schneider, M. F., Wixforth, A., and Guttenberg, Z. (2006). Acoustic mixing at low Reynolds numbers. *Applied Physics Letters*, 88:054102.

[Stoecklein and Di Carlo, 2019] Stoecklein, D. and Di Carlo, D. (2019). Nonlinear microfluidics. *Analytical Chemistry*, 91:296–314.

[Thameem et al., 2016] Thameem, R., Rallabandi, B., and Hilgenfeldt, S. (2016). Particle migration and sorting in microbubble streaming flows. *Biomicrofluidics*, 10:014124.

[Thameem et al., 2017] Thameem, R., Rallabandi, B., and Hilgenfeldt, S. (2017). Fast inertial particle manipulation in oscillating flows. *Physical Review Fluids*, 2:052001.

[Turkoz et al., 2018] Turkoz, E., Perazzo, A., Arnold, C., and Stone, H. (2018). Salt type and concentration affect the viscoelasticity of polyelectrolyte solutions. *Applied Physics Letters*, 112(20).

[Vázquez-Vergara et al., 2017] Vázquez-Vergara, P., Rojas, A. M. T., Guevara-Pantoja, P. E., Poiré, E. C., and Caballero-Robledo, G. A. (2017). Microfluidic flow spectrometer. *Journal of Micromechanics and Microengineering*, 27(7):077001.

[Vishwanathan and Juarez, 2019a] Vishwanathan, G. and Juarez, G. (2019a). Steady streaming flows in viscoelastic liquids. *Journal of Non-Newtonian Fluid Mechanics*, 271:104143.

[Vishwanathan and Juarez, 2019b] Vishwanathan, G. and Juarez, G. (2019b). Steady streaming viscometry of Newtonian liquids. *Physics of Fluids*, 31:041701.

[Vishwanathan and Juarez, 2019c] Vishwanathan, G. and Juarez, G. (2019c). Steady streaming viscometry of Newtonian liquids. *Physics of Fluids*, 31:041701.

[Vlassopoulos and Schowalter, 1993] Vlassopoulos, D. and Schowalter, W. R. (1993). Characterization of the non-Newtonian flow behavior of drag-reducing fluids. *Journal of Non-Newtonian Fluid Mechanics*, 49:205–250.

[Waigh, 2005] Waigh, T. A. (2005). Microrheology of complex fluids. *Reports on Progress in Physics*, 68:685–742.

[Waigh, 2016] Waigh, T. A. (2016). Advances in the microrheology of complex fluids. *Reports on Progress in Physics*, 79:074601.

[Wang et al., 2011] Wang, C., Jalikop, S. V., and Hilgenfeldt, S. (2011). Size-sensitive sorting of microparticles through control of flow geometry. *Applied Physics Letters*, 99:034101.

[Wang, 1968] Wang, C.-Y. (1968). On high-frequency oscillatory viscous flows. *Journal of Fluid Mechanics*, 32:55–68.

[Wang, 1989] Wang, C. Y. (1989). Exact solutions of the unsteady navier-stokes equations. *Applied Mechanics Reviews*, 42:269–282.

[Ward and Fan, 2015] Ward, K. and Fan, Z. H. (2015). Mixing in microfluidic devices and enhancement methods. *Journal of Micromechanics and Microengineering*, 25:094001.

[Wiklund et al., 2012] Wiklund, M., Green, R., and Ohlin, M. (2012). Acoustofluidics 14: Applications of acoustic streaming in microfluidic devices. *Lab on a Chip*, 12:2438–2451.

[Wilson and Poon, 2011] Wilson, L. G. and Poon, W. C. K. (2011). Small-world rheology: an introduction to probe-based active microrheology. *Physical Chemistry Chemical Physics*, 13:10617–10630.

[Wu et al., 2012] Wu, L., Guan, G., Hou, H. W., Bhagat, A. A. S., and Han, J. (2012). Separation of leukocytes from blood using spiral channel with trapezoid cross-section. *Analytical Chemistry*, 84:9324–9331.

[Xia et al., 2012] Xia, H. M., Wang, Z. P., Fan, W., Wijaya, A., Wang, W., and Wang, Z. F. (2012). Converting steady laminar flow to oscillatory flow through a hydroelasticity approach at microscales. *Lab on a Chip*, 12:60–64.

[Xie et al., 2015] Xie, Y., Chindam, C., Nama, N., Yang, S., Lu, M., Zhao, Y., Mai, J. D., Costanzo, F., and Huang, T. J. (2015). Exploring bubble oscillation and mass transfer enhancement in acoustic-assisted liquid-liquid extraction with a microfluidic device. *Scientific Reports*, 5.

[Yang et al., 2007] Yang, J., Chen, C., Hu, I. ., and Lyu, P. (2007). Design of a self-flapping microfluidic oscillator and diagnosis with fluorescence methods. *Journal of Microelectromechanical Systems*, 16(4):826–835.

[Yazdi and Ardekani, 2012] Yazdi, S. and Ardekani, A. M. (2012). Bacterial aggregation and biofilm formation in a vortical flow. *Biomicrofluidics*, 6:044114.

[Yeo and Friend, 2009] Yeo, L. Y. and Friend, J. R. (2009). Ultrafast microfluidics using surface acoustic waves. *Biomicrofluidics*, 3:012002.

[Zhou and Schroeder, 2016] Zhou, Y. and Schroeder, C. M. (2016). Single polymer dynamics under large amplitude oscillatory extension. *Physical Review Fluids*, 1:053301.

[Zia, 2018] Zia, R. N. (2018). Active and passive microrheology: theory and simulation. *Annual Review of Fluid Mechanics*, 50:371–405.

[Zilz et al., 2014] Zilz, J., Schäfer, C., Wagner, C., Poole, R. J., Alves, M. A., and Lindner, A. (2014). Serpentine channels: micro-rheometers for fluid relaxation times. *Lab on a Chip*, 14:351–358.

[Zimm, 1956] Zimm, B. H. (1956). Dynamics of polymer molecules in dilute solution: Viscoelasticity, flow birefringence and dielectric loss. *The Journal of Chemical Physics*, 24:269–278.